remote sensing

MDPI

Article

An Integrated Monitoring Concept for Dam Infrastructure: Operational PSI Service and Application of Electronic Corner Reflectors (ECR)

Jannik Jänichen [1,*], Jonas Ziemer [1], Carolin Wicker [2], Katja Last [2], Lieselotte Spieß [1], Jussi Baade [3], Christiane Schmullius [1,4] and Clémence Dubois [5]

[1] Department for Earth Observation, Institute of Geography, Friedrich Schiller University Jena, Leutragraben 1, 07743 Jena, Germany; jonas.ziemer@uni-jena.de (J.Z.)
[2] Department for Water Economy, Ruhrverband, Kronprinzenstraße 37, 45128 Essen, Germany
[3] Department for Physical Geography, Institute of Geography, Friedrich Schiller University Jena, Loebdergraben 32, 07743 Jena, Germany
[4] School for Climate Studies (SCS), Stellenbosch University, Stellenbosch 7599, South Africa
[5] Institute of Data Science, German Aerospace Center, Maelzerstraße 3-5, 07745 Jena, Germany
* Correspondence: jannik.jaenichen@uni-jena.de; Tel.: +49-3641-948924

Highlights

What are the main findings?

- The long-term analysis of Sentinel-1 backscatter demonstrates stable signal behavior of all installed electronic corner reflectors (ECRs) over more than 2.5 years (typical Amplitude Dispersion Index ≤ 0.4), confirming their suitability as highly coherent radar targets for Persistent Scatterer Interferometry (PSI).
- PSI analyses based on the ECR installations yielded millimeter-level deformation estimates that agree with in situ plumb and trigonometric measurements, with typical Root Mean Square Error (RMSE) values of 2 to 5 mm and correlations up to r = 0.7, confirming the reliability of ECR-based PSI under real-world operational conditions.

What are the implications of the main findings?

- ECRs enable PSI analyses at dams where conventional passive reflectors cannot be installed, providing comparable signal stability but requiring higher operational maintenance.
- The developed operational PSI service integrates ECR-based PSI results and ground-motion products into an accessible web platform, supporting dam operators with interactive time-series visualization, standardized downloads, and practical decision-making tools for infrastructure surveillance.

Academic Editors: Antonio Miguel Ruiz Armenteros, Roberto Tomás, Joaquim João Sousa, M. Clara de Lacy and Zhenhong Li

Received: 23 January 2026
Revised: 2 April 2026
Accepted: 15 April 2026
Published: 17 April 2026

Abstract

Long-term stability of dam infrastructure is crucial for flood protection, water resource management, and drinking water supply. In many regions, the increasing impact of climate change and structural aging necessitates advanced monitoring approaches for embankment and gravity dams. PSI has emerged as a valuable technique for detecting surface deformation rates with millimeter precision. This study presents a comprehensive monitoring concept that combines satellite-based PSI analyses with the first operational use of ECRs at dam sites in North Rhine-Westphalia (NRW), Germany. Over a period of more than two years, ECRs were observed under real-world conditions using Sentinel-1 data. Compared to traditional passive reflectors, ECRs offer improved signal stability and a compact design, making them particularly suitable for confined or sensitive dam

environments. The analysis of displacement time series confirms the suitability of ECRs for long-term deformation monitoring in complex dam settings. Intercomparison of two PSI time series demonstrated high internal consistency (correlation > 0.9, RMSE < 1 mm), while validation against in situ measurements confirmed millimeter-level agreement with RMSE values between 2 and 5 mm and correlations up to 0.7. In addition, a dedicated web-based platform was developed to provide processed ECR-based PSI results to dam operators, offering interactive visualizations, time-series access, and standardized downloads. This integration of advanced interferometric synthetic aperture radar (InSAR) methods, innovative hardware, and user-oriented service delivery marks a significant step toward operational dam monitoring using satellite remote sensing.

Keywords: dam monitoring; DInSAR; PSI; ground motion service; CR; ECR; Sentinel-1

1. Introduction

1.1. Motivation

Dams are critical infrastructures that play a central role in flood protection, water supply, hydropower generation, and regional water management. Ensuring their structural integrity is therefore essential for public safety and long-term operational reliability. Conventional dam monitoring relies on established in situ geodetic techniques such as plumb-line systems, trigonometric surveys, precise leveling, and, more recently, GNSS observations [1,2]. These methods provide high measurement accuracy at selected locations and are well integrated into regulatory frameworks and safety guidelines. However, they typically offer limited spatial coverage and, depending on the technique, relatively low temporal resolution, which can hamper the detection of spatially heterogeneous or evolving deformation patterns along dam bodies and abutments.

Satellite-based Earth observation has emerged as a valuable complement to classical monitoring approaches. In particular, multi-temporal interferometric synthetic aperture radar (MT-InSAR) techniques enable the detection of millimeter-scale surface deformations over large areas and long observation periods [3,4]. Persistent Scatterer Interferometry (PSI) has proven especially suitable for infrastructure monitoring due to its ability to extract stable deformation time series from coherent radar targets. Its capacity to provide spatially distributed measurements over extended observation periods makes it a particularly suitable complement to conventional in situ monitoring.

The increasing availability of analysis-ready satellite products has further facilitated the operational use of InSAR-based deformation monitoring. National and continental ground motion services, such as the German Ground Motion Service (Boden-Bewegungsdienst Deutschland, BBD) and the European Ground Motion Service (EGMS), provide standardized PSI products derived from Sentinel-1 data and offer a consistent framework for large-scale deformation monitoring [5–9]. Their application to dam infrastructure is discussed in the following sections.

1.2. State of the Art

A growing body of literature demonstrates the applicability of MT-InSAR and PSI for dam deformation monitoring. Numerous case studies have investigated both gravity dams and embankment dams of varying sizes, construction types, and environmental settings [1,10–23]. These studies show that PSI can capture long-term deformation trends and seasonal behavior, provided that sufficient radar coherence is available. At the same time, they highlight several limitations inherent to InSAR-based measurements, including sensitivity to line-of-sight (LOS) geometry, reduced observability of north–south motion

components, and the dependence on the availability and spatial distribution of coherent scatterers on dam surfaces.

To mitigate coherence limitations and improve measurement reliability, artificial radar targets have been widely employed in InSAR-based deformation monitoring. Passive corner reflectors (CRs) are the most established solution and have been used extensively in geodetic applications, landslide monitoring, and infrastructure surveillance [24–32]. In the context of dams and water infrastructure, CRs have been shown to significantly enhance persistent scatterer density and provide stable reference points for long-term deformation analysis [33–35]. Nevertheless, their deployment at dam sites is often constrained by practical considerations. Passive CRs are typically bulky, visually intrusive, and require careful installation and alignment. At dams, access restrictions, safety regulations, heritage protection, and limited available space can strongly limit where and how such reflectors can be installed. Recent developments in artificial radar target design include compact and polyhedral passive corner reflectors, which have been shown to improve deployability and angular response while maintaining high radiometric stability for Sentinel-1 InSAR applications [36,37]. These advances represent an alternative strategy to enhance InSAR observability through geometric optimization of passive reflectors.

In situ geodetic techniques remain the reference standard for dam monitoring and validation. GNSS measurements provide three-dimensional displacement information with high accuracy but require permanent installations, continuous power supply, and regular maintenance, and are therefore usually limited to a small number of discrete locations. Plumb-line systems and trigonometric surveys are well established in dam safety practice and deliver reliable long-term measurements, yet they offer sparse spatial sampling and are typically acquired at lower temporal frequency [1,2]. As a result, both satellite-based and in situ techniques exhibit complementary strengths and weaknesses. This complementarity motivates the integration of satellite-based PSI with artificial radar targets and ground-based validation, as pursued in the present study.

1.3. The Application Progress of ECRs in Dam Monitoring

Electronic corner reflectors (ECRs) represent a more recent development in the field of artificial radar targets. Unlike passive CRs, ECRs are active transponders that receive, amplify, and retransmit the radar signal, resulting in a strong and highly stable radar response. Previous research on ECRs has primarily focused on their use at geodetic calibration and test sites, where they have been shown to provide excellent radiometric stability and suitability for multi-temporal InSAR applications [38–43]. These studies demonstrated the potential of ECRs as coherent reference targets for deformation monitoring but were largely conducted under controlled or semi-controlled conditions rather than in operational infrastructure environments.

The application of ECRs to dam monitoring has so far remained limited. While their compact size and high signal stability make them attractive for deployment in confined or sensitive locations, systematic multi-year studies evaluating their performance at real dam structures are scarce. In particular, there is a lack of investigations that assess ECR-based PSI under operational conditions, compare the resulting deformation time series with established in situ measurements, and evaluate their suitability for routine dam monitoring workflows. As a result, the role of ECRs relative to passive CRs and conventional geodetic techniques in dam monitoring practice has not yet been comprehensively established.

This study addresses this gap by transferring electronic corner reflector (ECR) technology from calibration-oriented applications to real-world dam environments. Building on a preceding publication that detailed the methodology for ECR-supported multi-year PSI analyses at dam structures [44], the present work focuses on the resulting deformation measurements and their operational applicability. Multi-year PSI analyses are conducted

at several dam sites, and the derived deformation time series are validated against established plumb-line and trigonometric measurements.

Beyond the methodological and hardware-related aspects, dam operators increasingly require operational, analysis-ready, and explorable outputs rather than static deformation maps. While recent studies in Germany have assessed the suitability of BBD data for dam monitoring [10,45,46], no dedicated service integrating ECR-based PSI results with site-specific visualization and download capabilities for dam operators has been established. This represents a second key gap addressed by the present study.

Although several ground-motion services already exist, including the German Ground Motion Service (BBD) [5,6], the European Ground Motion Service (EGMS) [7], and the regional Ground Motion Service for North Rhine–Westphalia (Bodenbewegungskataster NRW provided by Geobasis NRW) [47], these platforms offer standardized, large-scale products that are not optimized for dam infrastructure and do not include ECR-based time series. To address this limitation, the service developed here complements these existing systems by providing site-specific PSI analyses, multi-year ECR time series, dam-focused layers, and a dedicated web interface designed for operational use by dam operators.

Overall, this paper presents an integrated monitoring concept that combines (i) multi-year PSI analyses supported by electronic corner reflectors with (ii) a specialized, web-based operational service. The results demonstrate that compact ECRs provide stable, high-quality targets for long-term PSI at dams, while the presented user-oriented platform has the potential to lower adoption barriers and support scalable, routine dam surveillance.

2. Study Area and Data

2.1. Study Area

This study focuses on selected reservoirs operated by the Ruhrverband in NRW, Germany [48], a non-profit water and reservoir management company under public law. The network includes gravity dams and embankment dams situated in complex topographic settings, with seasonal hydrometeorological variations that influence reservoir water levels and water pressure. Figure 1 illustrates the jurisdiction of the Ruhrverband and the locations of its major rivers and reservoirs. All ECRs that were deployed are additionally marked with red arrows.

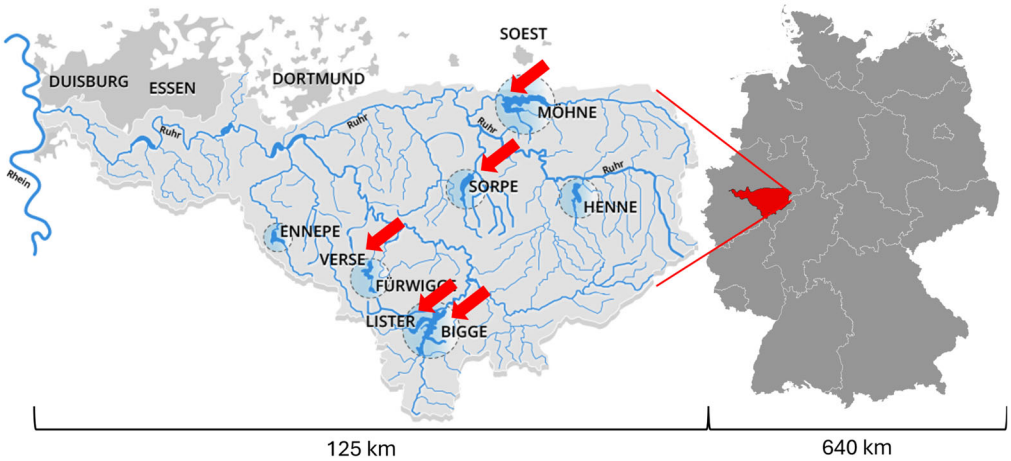

Figure 1. Catchment of the river Ruhr and jurisdiction of the Ruhrverband [48], including major reservoirs, and its location within Germany [49]. Deployed ECRs are indicated with red arrows. Six ECRs were installed across five dam structures. Two ECRs were deployed at the Bigge Dam, while one ECR was installed at each of the remaining dams.

Selection of the dams follows a previously developed suitability index that identifies appropriate structures and site locations for ECR installation [44]. This study extends earlier backscatter analyses by adding a PSI component. It covers five Ruhrverband reservoirs: two gravity dams (Möhne and Lister) and three embankment dams (Sorpe, Bigge, and Verse). The Möhne Dam, located in the Arnsberg Forest Nature Park, is 40 m high with a 650 m crest and plays a key role in regional water supply and flood control. The Lister Dam is 42 m high with a 264 m crest and functions as a forebay to the downstream Bigge reservoir, providing hydraulic buffering that helps interpret seasonal load-response patterns [50]. Figure 2 shows the five ECR sites.

The three embankment dams are equally important for catchment management but differ structurally and in their geometric interaction with the radar LOS direction. The Sorpe Dam is 60 m high with a 700 m long crest. The Bigge Dam, the largest structure in this study, is 52 m high with a 640 m long crest; two ECRs were installed to cover both abutments and support ascending and descending track coverage. The Verse Dam is 62 m high with a 320 m long crest, characterized by compact geometry and limited natural persistent scatterers.

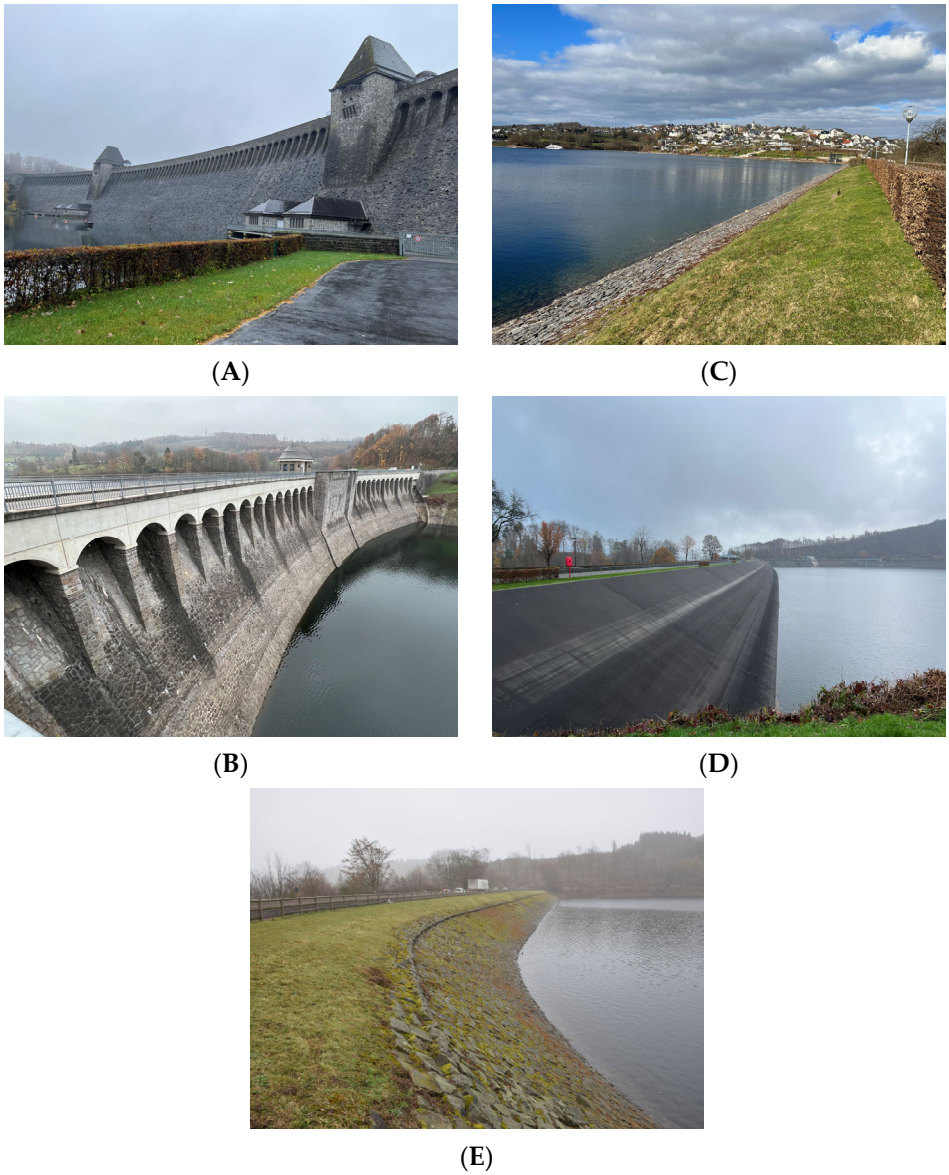

Figure 2. Overview of the five dams included in this study: gravity dams (**A**) Möhne, (**B**) Lister; embankment dams (**C**) Sorpe, (**D**) Bigge, (**E**) Verse. Photographs by the authors.

2.2. Data

2.2.1. Satellite Data

High-resolution LiDAR from the Geodata Infrastructure North Rhine-Westphalia (GDI NRW; 1 m) provided a digital elevation model (DEM) for detailed topographic mapping and for preprocessing of the Sentinel-1 data [51]. It was also used for subsequent PSI processing.

The satellite dataset (Table 1) consists of Sentinel-1 Single Look Complex (SLC) scenes [52]. Covering the full calendar years 2023 and 2024, the first observation window is extended by an additional half year into 2025, allowing an evaluation of whether a longer observation period improves PS coverage and stabilizes deformation estimates.

Table 1. Attributes of the Sentinel-1 data used in this study [52].

Data	Sentinel-1 Ascending	Sentinel-1 Descending
Number of scenes (01/2023–06/2025)	47–74	45–73
Temporal resolution (days)	12	12
Acquisition mode	Interferometric Wide Swath (IW)	Interferometric Wide Swath (IW)
Polarization	VV	VV
Wavelength	C-Band	C-Band
Relative orbit number	15	139
Frame	164	421

2.2.2. In Situ Measurements

The in situ datasets were supplied by the Ruhrverband [53–61] and consist of two primary geodetic monitoring techniques: plumb systems and trigonometric. Table 2 summarizes the spatial distribution and measurement cadence at each site.

Table 2. Measurement types, intervals, and point counts for in situ monitoring at the six dams from the Ruhrverband [53–61].

Dam	Dam Type	Plumb: Interval—No. Points	Trigonometry: Interval—No. Points
Möhne	Gravity Dam	daily—1	semi-annual—27
Lister		–	semi-annual—16
Sorpe	Embankment Dam	–	annual—10
Bigge		–	annual—13
Verse		–	annual—5

A plumb system is installed at the Möhne dam, where it provides daily radial deformation data. Trigonometric surveys are performed semi-annually at the gravity dams and annually at the embankment dams, yielding additional deformation data from 5 to 27 measurement points per structure. Figure 3 illustrates the distribution of geodetic measurement points along the Möhne Dam at three different elevation levels, serving as a representative example. The distribution of measurement points at the other dams is similar. The plumb line is located at the center of the dam [53]. Together, these in situ datasets provide spatially distributed and temporally consistent ground-truth information that is used to evaluate the accuracy and interpretability of the satellite-based PSI data.

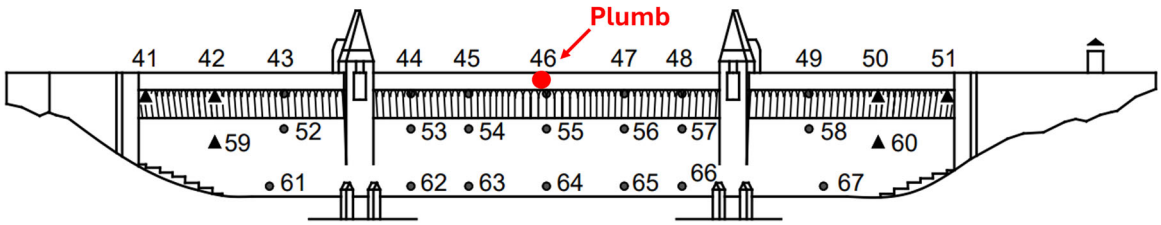

Figure 3. Observation points for horizontal and vertical displacements at the Möhne Dam, including the location of the plumb line. Vertically exaggerated by a factor of two [53].

3. Methods

Figure 4 illustrates the workflow of this study. The starting point is the methodology documented in the preceding publication, which resulted in the installation of ECRs at the dams described above, utilizing the CR Index, a spatial measure that is used identify optimal locations for ECR placement [44]. Before the PSI analysis, a renewed assessment of backscatter stability was conducted for these sites. The PSI results are then compared with and validated against the Ruhrverband's in situ data. Finally, all outputs, including the CR Index and related results [44], are integrated into an online service designed to help dam operators establish a comprehensive monitoring concept.

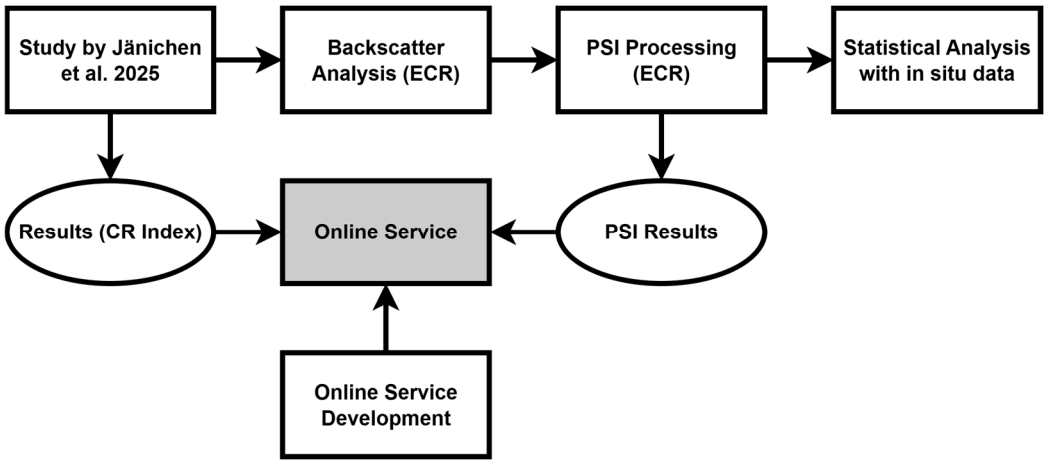

Figure 4. Simplified workflow of this study. Findings from the prior study [44] serve as the starting point for the extended backscatter and PSI analyses. All outputs are implemented in and made available through the online service.

3.1. Data Processing and Statistical Analysis

Data processing includes backscatter analysis and PSI analysis. Backscatter analysis follows the procedures documented in Jänichen et al. [44] and Ziemer et al. [62], with the observation period extended to two and a half years. The main steps include standard preprocessing [62] with targeted refinements in specific stages [62]. In detail, this includes applying the precise orbit file, splitting the TOPS sub-swaths, radiometric calibration to β^0, TOPS deburst, terrain flattening, and terrain correction. In addition, multilooking and a 3 × 3 boxcar filter were applied. After running these steps in the Sentinel Application Platform (SNAP), the backscatter values were converted to dB, exported, and analyzed statistically.

The PSI analyses presented in this study are generated using a dedicated processing chain based on the open-source StaMPS software (version 2), while the term "PSI service" refers to the operational framework for data handling, quality control, visualization, and delivery of analysis-ready results to dam operators. For the PSI analysis, the StaMPS

(Stanford Method for Persistent Scatterers) software package was used [63–71]. Sentinel-1 SLC stacks were preprocessed using the snap2stamps software package (version 2), which is based on SNAP to generate StaMPS-ready interferometric inputs: precise orbit application, thermal-noise removal and radiometric calibration, burst splitting and debursting, co-registration to a reference using back-geocoding and Enhanced Spectral Diversity (ESD), interferogram formation with DEM-assisted topographic phase removal, basic coherence screening, and export to StaMPS directory structure [64–66]. At the Möhne Dam, a prolonged malfunction of the installed ECR resulted in a significantly delayed start of the usable time series. Consequently, PSI processing for this site begins only in early 2024, which affects the temporal extent of the corresponding deformation plots and statistical comparisons. More generally, ECR malfunctions were identified by significant drops in backscatter amplitude below the expected operational level. Time series segments corresponding to inactive periods were excluded from PSI processing and statistical comparisons. The resulting data gaps are documented in the backscatter time series plots (Figure 5) and their impact on temporal coverage is noted in the results.

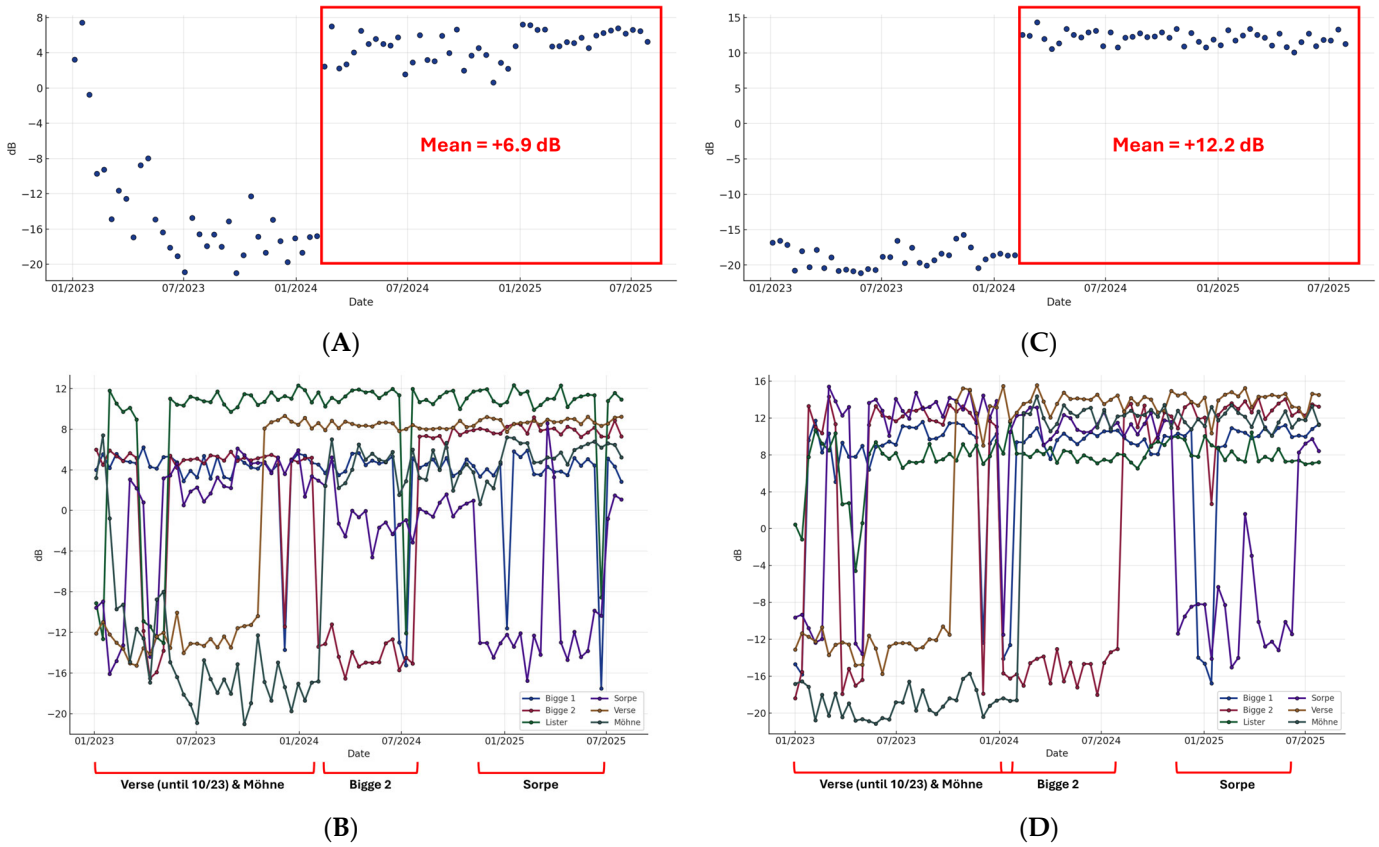

Figure 5. Example results of the backscatter analysis for the Möhne Dam in the (**A**) ascending and (**C**) descending orbits. Panels (**B**,**D**) show the corresponding backscatter time series for all analyzed dams (Bigge 1, Bigge 2, Lister, Sorpe, Verse, and Möhne) for the ascending and descending orbits, respectively. Periods of stable, high backscatter indicate operational electronic corner reflectors (ECRs). Data gaps, characterized by abrupt drops in backscatter to values between −12 and −16 dB, are explicitly highlighted by red brackets below the plots. Each time series in panels (**B**,**D**) is labeled with the corresponding dam name.

The StaMPS workflow included the selection of PS candidates using the Amplitude Dispersion Index (ADI), iterative estimation of DEM error and atmospheric phase screen, phase unwrapping, and inversion for LOS velocities and displacement time series relative to a stable reference point [68]. PS candidates were selected using a conservative ADI

threshold (ADI ≤ 0.25), which follows commonly adopted values in PSI processing for ensuring high phase stability and reliable point selection [67]. This threshold was applied uniformly throughout the processing to ensure stable point identification prior to network formation and phase unwrapping.

Processing targeted two intervals, 2.0 years (24 months) and 2.5 years (31 months), in order to evaluate whether extending the observation period improves PS density, time-series stability, and overall agreement with in situ measurements. Point quantity was evaluated via PS density and spatial coverage, and quality was assessed by agreement with the available independent in situ measurements (e.g., correlation and RMSE). Both intervals used identical processing settings, including the two-pass ADI thresholds (0.40 initial, 0.25 refinement), to ensure comparability.

The ECRs were operated within their specified temperature range, and no explicit hardware- or model-based temperature compensation was applied in the PSI processing. For the processing, default values were largely used, with only minor adjustments applied, in order to adapt the processing to the small-scale characteristics and specific conditions of dam structures. These adaptations are presented in Table 3.

Table 3. Default and adjusted values during StaMPS Processing [68]. The parameters ref_centre_lonlat and ref_radius have to be adapted individually for every dam. Reference points were selected based on visual inspection of the PS network and local knowledge of the dam structure, prioritizing locations with high temporal coherence, absence of known deformation, and stable backscatter behavior. Where possible, reference points were placed on stable, non-deforming infrastructure elements adjacent to the dam body.

Value	Description	Default Setting	Adapted Setting
ref_centre_lonlat	Center coordinate reference point	-	individual
ref_radius	Radius surrounding reference point (m)	-	individual
scla_deramp	Phase ramp estimation for each interferogram	n	y
weed_neighbours	Flag for proximity weeding	n	y
max_topo_err	Maximum uncorrelated DEM error (m)	20 m	5 m
select_reest_gamma_flag	Re-estimating PS selection	y	n

The selection of non-default StaMPS parameters, in particular the reduced max_topo_err threshold, reflects a conservative processing strategy tailored to ECR-based PSI. Rather than maximizing PS density, the focus is placed on minimizing sidelobe effects and ensuring a clear spatial association between the identified PS and the physical reflector location. Previous methodological work demonstrated that relaxed max_topo_err thresholds can increase the number of detected PS candidates around strong artificial reflectors but may also introduce spatially offset points and increased phase noise. Based on these findings, a stricter threshold was adopted to prioritize deformation reliability and interpretability over point quantity.

After comparing the two PSI time series (two years vs. two and a half years), they were spatially matched with trigonometric object points based on the nearest location for the subsequent statistical analysis. For the Möhne dam, statistical comparisons between PSI and plumb measurements were also carried out. If measurements were not acquired on the same day, the nearest temporal observation was used. For each site, descriptive statistics were computed: RMSE, mean bias, and Pearson's correlation coefficient (r). Visual comparisons included overlaid time-series plots to check for seasonality or drift.

When comparing PSI-derived deformation time series with in situ measurements, differences in measurement geometry must be considered. The decision not to apply geometric transformations is based on the following reasoning. PSI provides displacement measurements in the LOS, whereas plumb-line data represent radial deformation of the

dam body, and trigonometric measurements record horizontal displacement components. These quantities are therefore not directly equivalent. A fully consistent comparison would require projecting the in situ measurements into the LOS direction or decomposing the PSI results into vertical and horizontal components. Such geometric transformations were not applied in this study. Instead, the comparison is intended as a consistency and plausibility assessment, focusing on the temporal behavior, stability, and order of magnitude of the deformation signals rather than on a strict component-wise equivalence of displacement values. This approach reflects common practice in infrastructure monitoring studies where heterogeneous measurement geometries are combined to assess overall deformation behavior, as demonstrated in comparable PSI-based dam monitoring studies that report validation statistics under analogous geometric constraints [10,15,17]. While the measurement geometries are not identical, the dominant deformation direction at dam structures is typically oriented approximately perpendicular to the dam axis and toward the downstream direction. For the investigated sites, this dominant deformation component is not orthogonal to the Sentinel-1 LOS geometry, such that the satellite measurements capture a substantial fraction of the expected deformation signal. Specifically, as shown by Ziemer et al. [45], the projection of radial dam deformation into the Sentinel-1 LOS yields attenuation factors of approximately 0.3–0.6 for ascending tracks and 0.2–0.5 for descending tracks at the investigated dams, indicating that a meaningful fraction of the physical displacement is captured despite the geometric constraints. Consequently, despite the inherent geometric limitations, the comparison remains meaningful for evaluating consistency between satellite-based and in situ observations, provided that the validation statistics are interpreted accordingly.

3.2. Web-Based Service

In order to facilitate the retrieval of the results, a web-based Service was developed, including the results documented in Jänichen et al. [44]. The web service provides standardized PSI products through a lightweight, browser-based application built with HTML/CSS and JavaScript using Leaflet.js for mapping and Chart.js for interactive time-series plots [72]. Point data (PSI measurements with time series) are integrated as GeoJSON and displayed as clickable markers with popups, while raster products are published as XYZ tiles (PNG) exported from QGIS/GDAL. The service includes the CR Index as both raw and classified traffic-light layers, which indicate the suitability of specific locations for installing electronic corner reflectors, as well as the Land-Use Index (LUI), which highlights land-cover conditions that influence PSI coherence and reflector performance [42]. Users can toggle overlays, adjust transparency, view a dynamic legend, rotate the map, and work with a small-scale map for orientation.

For analysis and reporting, the application supports one-click downloads of a point's time series and chart image, a polygon-based bulk export for many points at once, and a side-by-side comparison of two locations with basic statistics. Shareable URLs capture the current map view (center, zoom, active layers), and a simple print/screenshot workflow helps produce figures for reports. The download files are structured in standardized, machine-readable formats that can be ingested directly into the Ruhrverband's monitoring system and can be adapted easily to other operators' data schemes, minimizing the need for additional post-processing.

The workflow is designed to be easily extensible. Operators can add their own datasets as files that appear directly within the map, clearly separated from standard layers. In addition, Python (3.13) helper scripts are provided to validate and convert new inputs, update the data index, and optionally add derived, motion-decomposed products. These scripts automate the ingestion workflow: operators place new PSI or raster files into a designated folder, run a single command that checks file integrity and naming

conventions, converts the data into the required GeoJSON or tile format, and updates the configuration so that the new layers appear automatically in the web application. Based on recent project findings [43], radial motion conversions are not universally meaningful; therefore, LOS remains the default representation, with optional motion components offered only where they add value and are clearly labeled.

Deployment follows a static hosting model, which keeps operations simple and reproducible: the app runs in any modern browser, serving tiles and GeoJSON files without a custom backend. In summary, the stack consists of JavaScript (Leaflet.js, Chart.js) for the client, GeoJSON and XYZ tiles for data delivery, and Python for preprocessing, conversion, and user data ingestion, enabling an efficient, reproducible, and operator-friendly way to deliver combined point and raster geoinformation. This enables the web-based service to provide a meaningful contribution for dam operators within a DIN-based monitoring framework [73].

4. Results

4.1. Backscatter Analysis

The backscatter analysis forms the basis for assessing whether the installed ECRs provide a sufficiently strong and stable radar signature for PSI processing. Prior to installation, the dam surface exhibits low and spatially variable backscatter (typically −8 to −20 dB), whereas the activated ECRs produce a strong, distinct trihedral response of up to 12 dB. This ensures the robust detection of persistent scatterers and supports the generation of long-term deformation time series.

The long-term stability of the ECR signature is reflected in the low ADI values and narrow temporal backscatter ranges over both the 24- and 31-month processing periods (Figure 5B,D). These metrics demonstrate a consistently stable radar response and confirm the suitability of the ECRs as reference targets for PSI. The absolute change in backscatter amplitude before and after commissioning is shown in Figure 5A,C. Table 4 additionally lists descriptive statistic parameters and ADI for each analyzed dam.

Across the six ECR sites (Bigge 1, Bigge 2, Lister, Sorpe, Verse, Möhne), the backscatter time series are consistently high and temporally stable over the observation period, as shown by the figures and the accompanying summary statistics (Table 4). In the ascending geometry, site-wise mean values span roughly 2 to 8.8 dB, while in the descending geometry, they range from about 8 to 16 dB. Descending amplitudes are higher than ascending at most sites, the Lister site being a notable exception. Across all records, observed amplitudes cover a broad domain from approximately −21 dB (lowest) to 15.5 dB (highest), with extended transmission gaps clearly visible as abrupt drops to −16 to −22 dB followed by a return to prior levels.

Figure 5A,C illustrate the backscatter time series at the ECR location on the Möhne Dam. The comparison contrasts the period before and after the activation of the ECR. In the ascending track, the mean backscatter at the ECR pixel increases by 6.9 dB after installation, while in the descending track, it increases by 12.2 dB and then remains at a high, stable plateau. Comparable increases are observed at the other ECR sites.

The ADI indicates generally low dispersion for the majority of series, with typical values in the order of below 0.4 at the most stable sites and elevated values where the records include longer low-amplitude intervals. Overall, ADI magnitudes span approximately 0.04 to 0.4, with the Lister Dam representing an exception in the ascending track, and 0.1 to 0.4 in the descending track. An exception is the Sorpe Dam in the ascending track, where markedly greater dispersion is observed alongside a higher number of transmission outages. Amplitude differences of 1–2 dB between individual observations or viewing geometries are small relative to the typically high ECR signal levels and do not affect the overall assessment of ECR stability.

Table 4. Statistical analysis of the backscatter analysis. Listed are statistical metrics and the ADI.

Dam	Flight Geometry	Number Scenes	Mean	Median	Minimum	Maximum	ADI
Möhne	Ascending	47	4.83	5.01	0.62	7.40	0.36
	Descending	45	12.11	12.19	10.06	14.34	0.07
Sorpe	Ascending	55	1.70	1.58	−4.61	8.58	1.55
	Descending	53	11.99	12.14	8.27	15.41	0.14
Bigge 1	Ascending	74	4.49	4.52	2.83	6.22	0.17
	Descending	71	9.82	9.97	5.08	11.72	0.12
Bigge 2	Ascending	59	6.53	7.12	4.21	9.18	0.22
	Descending	53	12.41	12.60	8.87	14.31	0.09
Lister	Ascending	71	11.05	11.04	8.95	12.31	0.06
	Descending	73	8.19	7.96	6.53	11.56	0.12
Verse	Ascending	54	8.55	8.59	7.74	9.31	0.04
	Descending	55	13.75	14.01	9.01	15.54	0.08

4.2. Comparative PSI Analysis and Validation

The comparison of the 24- and 31-month PSI solutions aims to assess the internal consistency of the deformation estimates. Both datasets represent the same ECR installations but differ in temporal coverage; agreement between them therefore indicates stable processing, robust ECR coherence, and reproducible displacement patterns over time.

Using the PSI analysis performed in StaMPS, all installed ECRs were identified as PS, and their deformation over the study period was computed. Figures 6 and 7 present, for the ascending and descending tracks, respectively, the ECR deformation profiles for analysis windows of 24 months and 31 months. In addition, several descriptive statistics are shown for comparison and summarized in detail in Table 5.

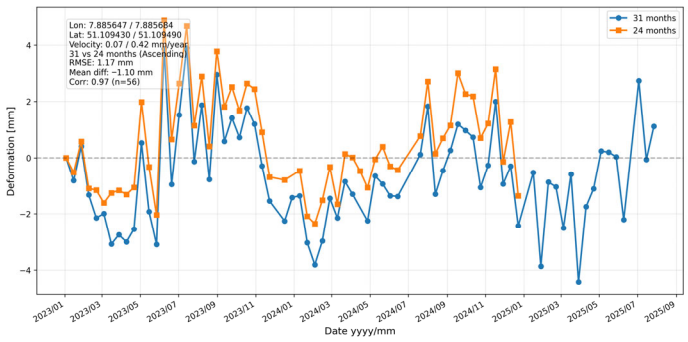

(**A**)

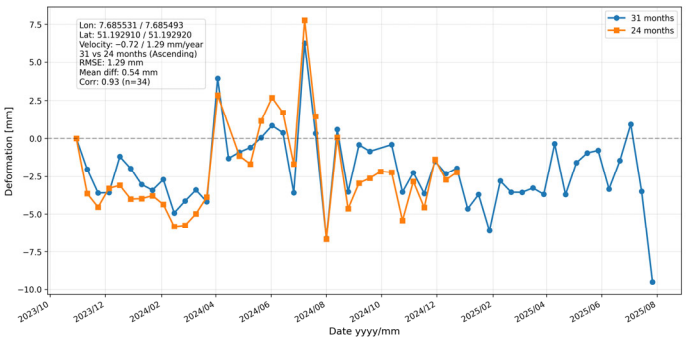

(**D**)

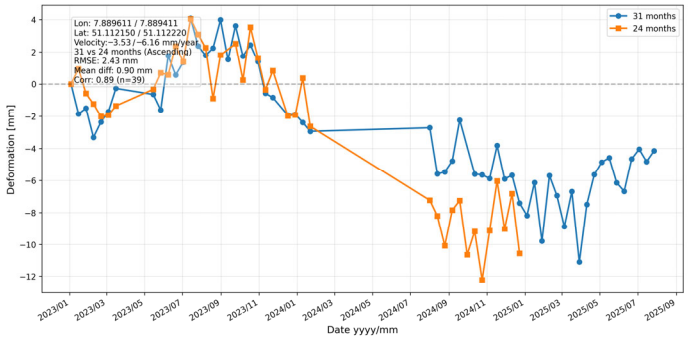

(**B**)

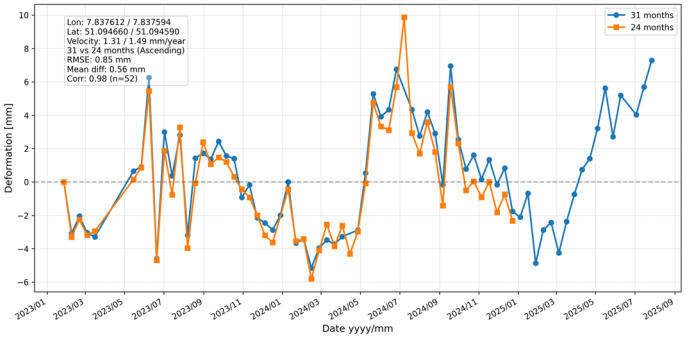

(**E**)

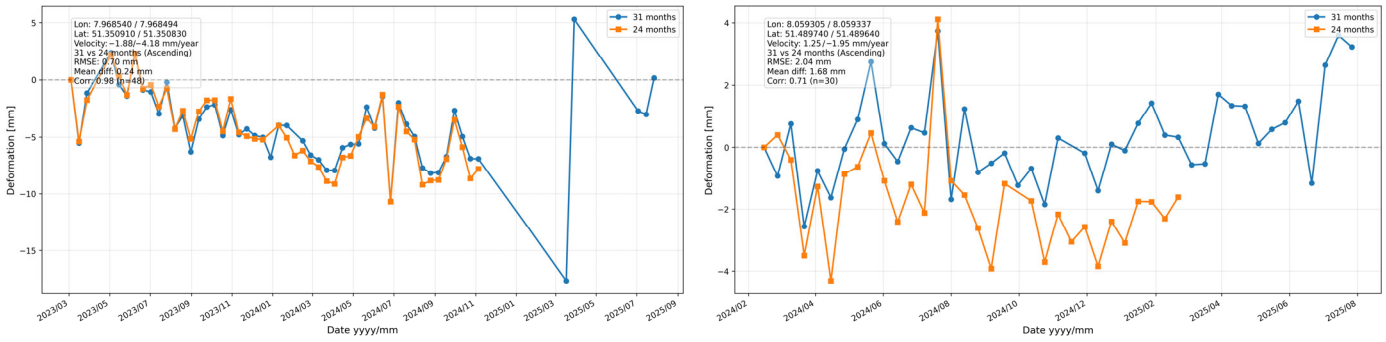

(**C**) (**F**)

Figure 6. LOS deformation for each analyzed ECR in the ascending orbit, with summary statistics. Linear interpolation was applied between acquisition dates to visualize the temporal evolution, which also explains the visually continuous segments across data gaps. Orange lines indicate the 24-month time series, blue lines the 31-month time series. Inset statistics refer to the comparison between the two observation windows. (**A**) Bigge 1; (**B**) Bigge 2; (**C**) Sorpe; (**D**) Verse; (**E**) Lister; (**F**) Möhne.

In most cases, the deformation time series for the 24-month and 31-month period show very similar temporal behavior and largely consistent seasonal patterns. This close agreement is reflected in low RMSE values (typically below 0.5 mm) and high correlations (>0.9) across most ECR sites, although small residual differences remain visible even during months covered by both observation windows. In particular, Bigge 1, Bigge 2, and Lister illustrate the typical seasonal behavior for dams (Table 5). Larger data gaps are present at Bigge 2 and Sorpe due to temporary ECR device outages, which correspond to the low-backscatter periods identified in Figure 5. In addition, the ECR installed on the Möhne dam wall became operational considerably later than the other ECRs, which explains the different x-axis in Figure 6. In the ascending track, Bigge 2 and Verse show poorer agreement between the 24- and 31-month deformation histories. For both sites, the PS points linked to the ECR are not located at exactly the same pixel but only differ a few meters in azimuth and/or range direction between the two observation windows. This is attributable to slight differences in the interferogram networks, atmospheric phase screen estimation, and phase unwrapping paths between the two processing windows, which can cause an adjacent pixel (often a sidelobe of the ECR) to be selected as the most coherent scatterer rather than the central ECR pixel. In contrast, the spatial locations of the ECR-associated PS at the other dams coincide to within approximately one pixel (≤3 m).

The descending-track deformation profiles show similar results, with similar data gaps due to ECR outages. Here as well, the two analysis periods for Bigge 2 and Verse show larger visual and statistical differences compared to the other four ECRs. For Lister, a lower correlation is observed in the descending geometry (r = 0.406), which is attributable to orbit-dependent geometric projection effects: although the dominant deformation component of the north–south oriented dam is directed east–west and is in principle well observable by Sentinel-1, the ascending and descending tracks project this component differently onto their respective LOS directions, which can lead to systematic differences in the observed deformation amplitudes and temporal patterns between orbits. The limited number of trigonometric survey epochs available for Lister further increases statistical uncertainty. For Sorpe, the descending RMSE of 2.05 mm combined with a high correlation (r = 0.947) indicates good agreement and does not represent a meaningful inconsistency. In the remaining cases, both the temporal patterns and the statistics mostly agree. The annual cycle is less observable in the descending track. In both viewing geometries,

the PSI analysis was successful and identified more than one point per ECR. Sidelobes were also identified, with locations that vary by dam.

Figure 7. LOS deformation for each analyzed ECR in the descending orbit, with summary statistics. Orange lines indicate the 24-month time series, blue lines the 31-month time series. Linear interpolation was applied between acquisition dates; inset statistics refer to the comparison between the two observation windows. (**A**) Bigge 1; (**B**) Bigge 2; (**C**) Sorpe; (**D**) Verse; (**E**) Lister; (**F**) Möhne.

Table 5. Statistical analysis of the ECR deformation. Listed are summary metrics for comparing the two deformation time series for both satellite orbits (ascending and descending), along with the standard deviations of each series.

ECR	Orbit	RMSE (mm)	MAE (mm)	Correlation	*p* Value	Std. Dev. 24 (mm)	Std. Dev. 31 (mm)
Bigge 1	Ascending	1.17	1.10	0.973	7.3493×10^{-36}	1.77	1.73
	Descending	0.23	0.19	0.989	8.8265×10^{-44}	1.61	1.57
Bigge 2	Ascending	2.43	1.83	0.892	2.3735×10^{-14}	3.67	4.72
	Descending	6.65	4.65	−0.381	2.6347×10^{-3}	3.58	3.70
Sorpe	Ascending	0.70	0.57	0.980	4.3457×10^{-34}	3.55	3.09
	Descending	2.05	1.62	0.947	2.8716×10^{-24}	3.58	3.61

Verse	Ascending	1.29	1.10	0.926	4.3746×10^{-15}	2.49	2.99
	Descending	4.16	3.42	0.161	3.5460×10^{-1}	1.72	2.10
Lister	Ascending	0.85	0.71	0.980	9.8046×10^{-37}	3.27	3.18
	Descending	3.53	3.16	0.406	2.5511×10^{-3}	2.38	2.38
Möhne	Ascending	2.04	1.83	0.708	1.1966×10^{-5}	1.43	1.65
	Descending	1.15	0.78	0.924	3.0423×10^{-13}	2.67	2.74

The validation of the PSI-derived deformations against in situ measurements is summarized in Table 6 and illustrated in Figure 8 for the ascending geometry (Figure A1 for the descending geometry in the Appendix A), as well as in Figure 9 for the Möhne Dam using plumb-line data. For the trigonometric surveys, only a small number of measurement epochs is available (typically fewer than ten dates per dam), and no temporal interpolation of in situ deformations was applied. Instead, PSI values were compared to the nearest available survey date. The resulting validation statistics are therefore based on a limited sample and should be interpreted with caution.

In the ascending tracks, the PSI and trigonometric time series align closely at most sites. Increases and decreases occur largely synchronously within a seasonal cycle, with maxima and minima showing consistent seasonal patterns and comparable deformation amplitudes, and only minor lateral offsets between the time series. Across several sites, the trigonometric measurements show consistently higher deformation amplitudes than the PSI-derived values. This systematic offset is visible in the overlaid time series but varies by dam and observation geometry.

Individual longer data gaps appear as interrupted segments or sparser point clouds, without substantially affecting the overall impression of close correspondence. In the descending geometry, visible deviations occur more frequently: the time series diverge over certain intervals, the scatter of differences around the reference line increases, and seasonal fluctuations appear locally attenuated. This pattern is reflected in the summary statistics presented in Table 6.

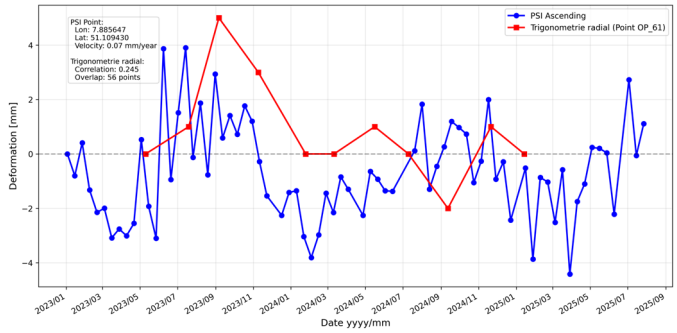

(**A**)

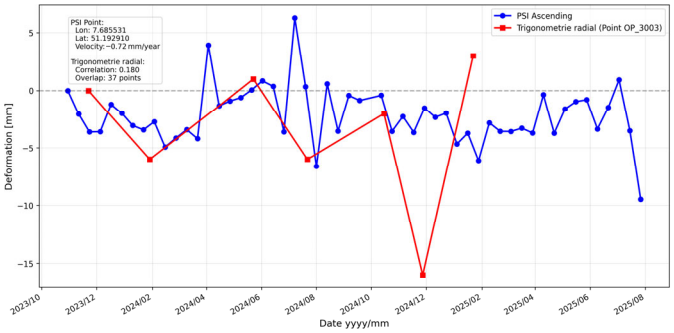

(**D**)

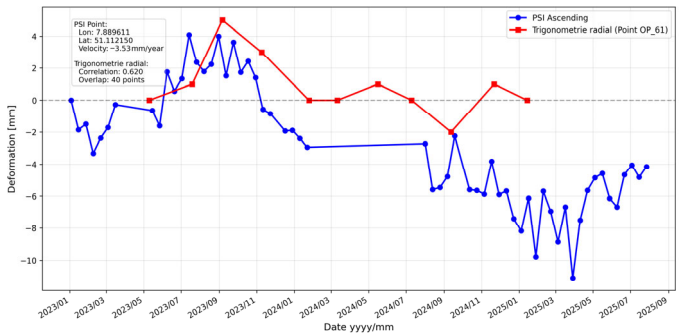

(**B**)

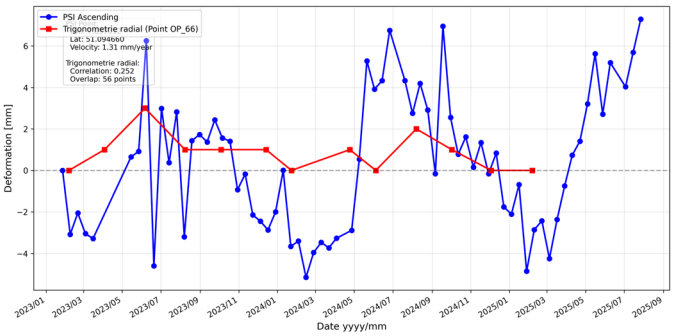

(**E**)

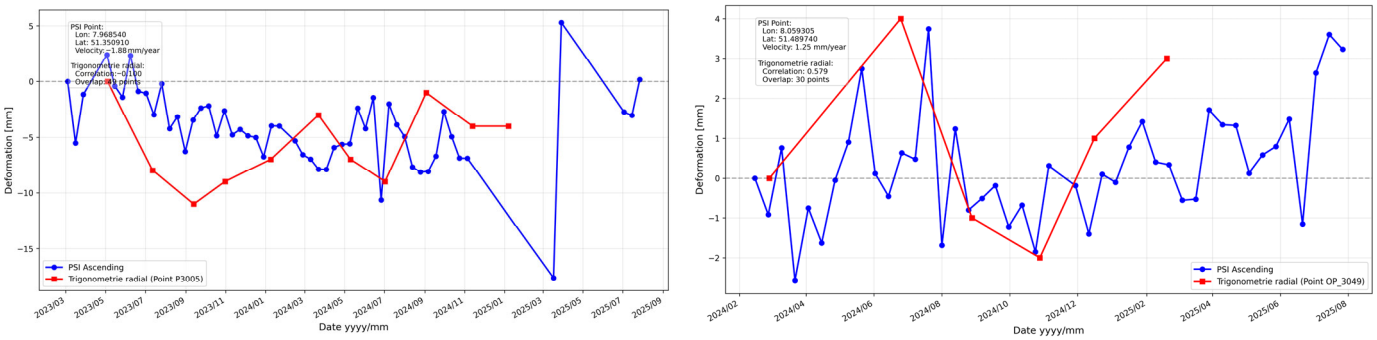

(**C**) (**F**)

Figure 8. Ascending-track LOS deformation of the analyzed ECRs, statistically validated against trigonometric measurements; summary statistics of agreement are included. Blue lines show PSI-derived deformation, orange markers indicate trigonometric survey epochs. Inset statistics (RMSE, r) refer to the PSI–trigonometric comparison. (**A**) Bigge 1; (**B**) Bigge 2; (**C**) Sorpe; (**D**) Verse; (**E**) Lister; (**F**) Möhne.

Table 6. Statistical validation of ECR deformations using trigonometric measurements. Summary metrics comparing the PSI-derived LOS and trigonometric deformation time series for both satellite orbits (ascending/descending) are reported. Note that the two datasets do not refer to the same geometry; the reported metrics should therefore be interpreted as indicators of temporal consistency rather than strict accuracy estimates.

ECR	Orbit	RMSE (mm)	MAE (mm)	Correlation	*p* Value
Bigge 1	Ascending	2.27	2.10	0.467	1.4797×10^{-1}
	Descending	7.34	6.83	0.087	7.9968×10^{-1}
Bigge 2	Ascending	3.81	3.31	0.649	3.0685×10^{-2}
	Descending	4.16	3.08	0.421	2.2549×10^{-1}
Sorpe	Ascending	4.61	4.11	0.483	8.0919×10^{-1}
	Descending	4.02	3.09	0.097	7.6534×10^{-1}
Verse	Ascending	3.66	3.34	0.493	2.1452×10^{-1}
	Descending	3.45	2.42	0.123	7.7194×10^{-1}
Lister	Ascending	3.30	2.93	0.575	3.9614×10^{-2}
	Descending	7.37	6.69	0.158	6.0514×10^{-1}
Möhne	Ascending	1.14	0.91	0.442	4.9684×10^{-3}
	Descending	5.87	4.36	−0.134	8.0077×10^{-1}

Figure 9 shows the comparison with the daily plumb line measurements for the Möhne Dam. Since PSI measures in LOS geometry, ascending and descending time series may show opposite patterns when deformation contains a strong horizontal component. This expected contrast is only partly visible in the present case. The high temporal resolution of the plumb data allows for a detailed tracking of the deformation patterns. Both datasets display consistent medium-term trends and characteristic plateaus. At the Möhne Dam, the time series begins only in early 2024, consistent with the delayed availability of a functioning ECR. The comparison with plumb-line measurements shows that the descending geometry exhibits a visually stronger agreement than the ascending geometry. Nevertheless, these statistics must be interpreted with caution because the PSI values represent LOS displacement, whereas the plumb line records radial deformation. The differences in measurement geometry influence both amplitude and correlation and can therefore affect the RMSE values reported here (ascending = 2.10 mm; descending = 2.89 mm; correlation ascending = 0.65; descending = 0.10).

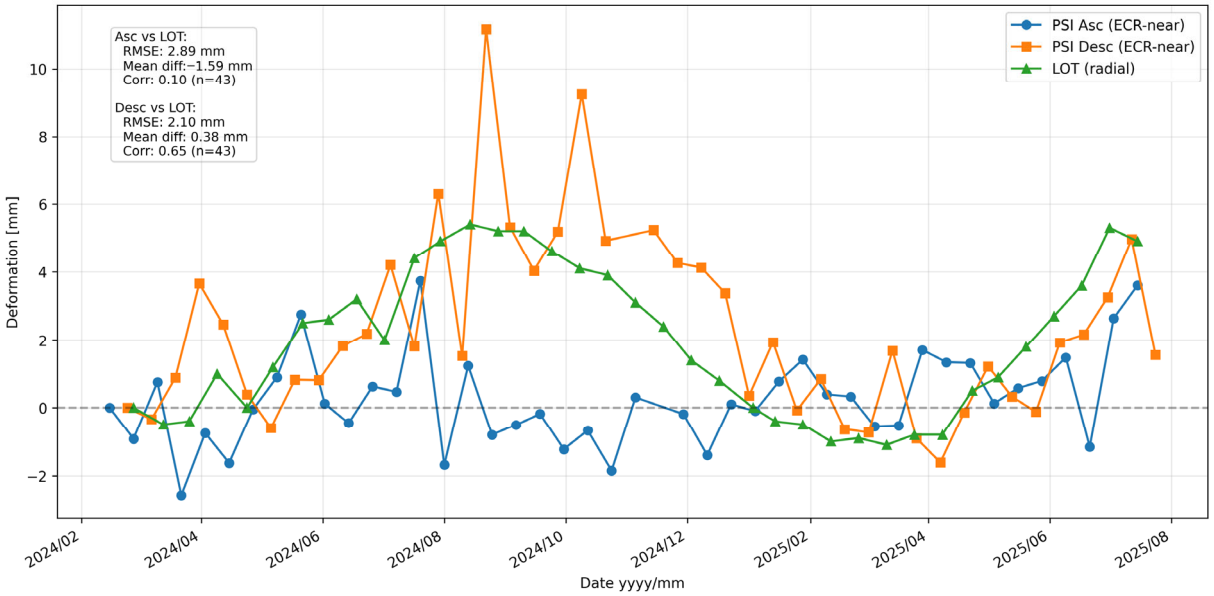

Figure 9. LOS deformation of the analyzed ECR at the Möhne Dam in the ascending and descending tracks, statistically validated against plumb measurements; summary statistics of agreement are included.

4.3. Web-Based Application and Data Accessibility

Figure 10 shows the user interface and several core functions of the web-based service. Figure 10A provides an overview of the Ruhrverband study area, which also serves as the default start extent. The map layout is easy to use and includes adaptive elements such as a dynamic legend, a small-scale map, and per-layer transparency controls for targeted interaction.

Figure 10B illustrates the download functionality, which supports bulk download for freely selectable, user-defined areas as well as single-point downloads, as shown in Figure 10C,D. For a single PS point (Figure 10C), the associated time-series chart can also be downloaded. The same applies to the comparison of two PS points (Figure 10D), where descriptive statistics are additionally provided to enable direct comparisons between different parts of a dam or, for example, between two points from different viewing geometries (ascending/descending).

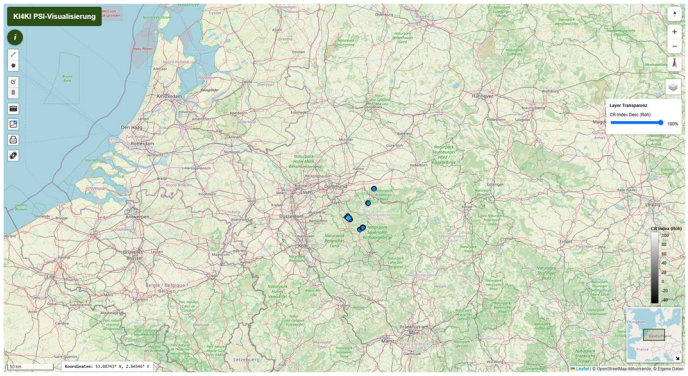

(**A**)

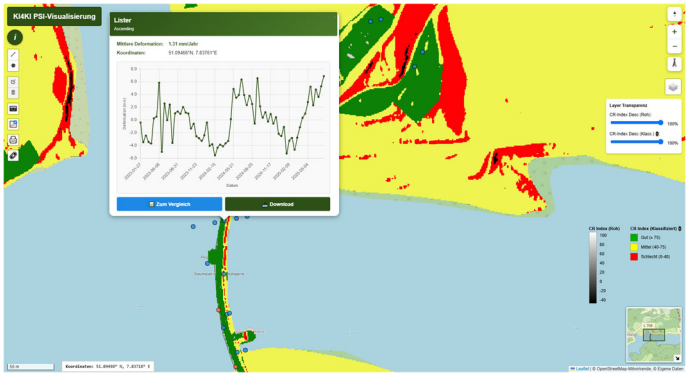

(**C**)

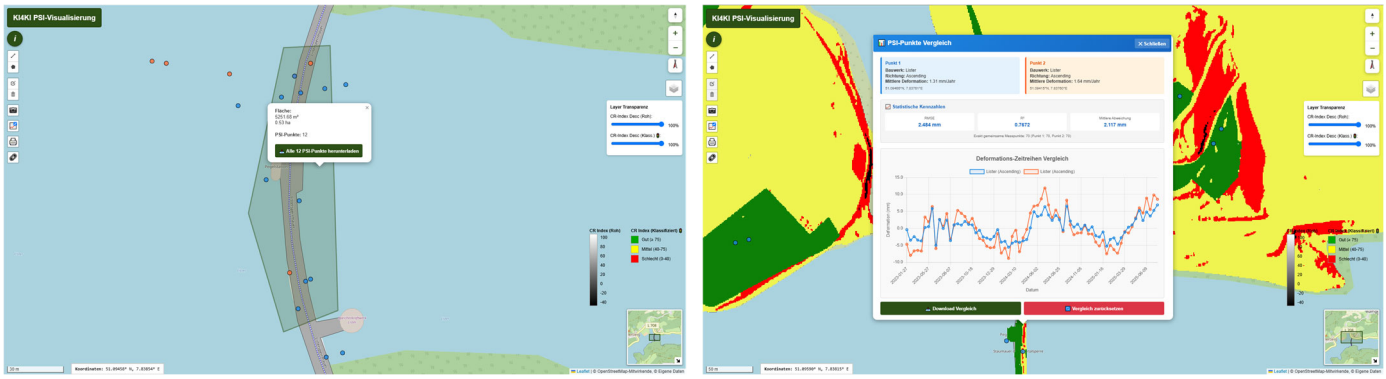

(**B**) (**D**)

Figure 10. Overview of the main functions (**A**) General overview, (**B**) Bulk download (**C**) PS illustration and download, (**D**) PS comparison and download.

5. Discussion

5.1. Assessment of Amplitude Stability

A meaningful PSI analysis over multiple years requires high temporal coherence. For the ECR time series, assessing signal stability is therefore essential and must precede the interpretation of deformation values. As shown in Section 4.1, the activated ECRs provide a strong and clearly distinguishable trihedral signature that remains consistently stable over time, whereas the surrounding dam surfaces exhibit substantially lower and more variable backscatter levels, reflected by the background backscatter observed during periods when the ECRs are inactive (Figure 5). Beyond this general contrast, several systematic differences between ascending and descending tracks emerge. Atmospheric conditions at the time of the Sentinel-1 overpasses may contribute to the offsets observed between ascending and descending backscatter levels in the ECR time series (Figure 5). The descending acquisitions take place in the morning, while ascending passes occur in the evening, a timing difference known to influence backscatter in vegetation and surface-moisture studies [74,75].

However, several-decibel differences between the two tracks are also consistent with acquisition geometry. Differences in incidence and azimuth angles including azimuthal anisotropy effects, can introduce systematic track-dependent offsets in Sentinel-1 backscatter time series [76,77]. The magnitude of these geometry-related effects depends on the applied radiometric processing. When backscatter is normalized to γ^0 and radiometrically terrain-corrected, the influence of incidence angle and local topography is reduced. In contrast, β^0 or σ^0 products without angular normalization retain a stronger dependence on viewing geometry, which can lead to persistent per-track backscatter offsets [78]. Given the high radiometric accuracy and long-term stability of Sentinel-1, such persistent differences between ascending and descending backscatter levels are therefore more plausibly explained by acquisition geometry and normalization choices than by instrumental drift [79,80].

For ECRs, boresight alignment and orientation relative to each track may additionally favor one viewing geometry, affecting the effective Radar Cross Section (RCS) and thus the amplitude levels [81,82]. Weather-related perturbations are expected primarily during precipitation events and are unlikely to explain long-lived track-wise differences on their own [83]. In summary, the consistently high signal levels and low dispersion values observed for all ECR installations indicate excellent conditions for subsequent PSI analysis and provide a robust basis for interpreting the deformation time series presented in Section 4.2.

5.2. Assessment of Deformation Quality

The results presented in Section 4.2 demonstrate high internal consistency of the ECR-derived PSI time series across both observation windows and both viewing geometries. This consistency is in line with the millimeter-level sensitivity reported in the InSAR literature for infrastructure monitoring under comparable processing standards, where key influencing factors include PS selection, network formation, referencing, and atmospheric correction [84]. The following discussion interprets the observed deformation patterns and orbit-dependent differences in the context of these established findings.

As shown in Section 4.2, the PSI displacement time series from the 24- and 31-month processing windows exhibit very high agreement, indicating that the ECR-derived signals are stable across different temporal extents and scene counts. The small residual differences between the 24- and 31-month solutions, including periods with overlapping acquisitions, are to be expected. They arise from the use of slightly different interferogram networks, variations in reference-point selection, differences in atmospheric phase estimation, and minor deviations in unwrapping paths. These factors lead to subtle, but methodologically consistent, differences in the reconstructed phase histories despite the overall high agreement. A slight drift between the 24- and 31-month solutions is visible at the Möhne ECR. This behavior is expected because the ECR became operational considerably later than at the other sites, resulting in a shorter effective time span, sparser early time interferogram connections, and a different Atmospheric Phase Screen (APS) estimation. Together with changes in reference-point selection and unwrapping paths between the two windows, these factors can introduce small systematic offsets despite high overall consistency. This internal consistency provides a solid basis for interpreting the remaining differences observed between ascending and descending tracks, which mainly reflect geometry-driven projection effects rather than processing uncertainty.

The conservative StaMPS parameter configuration adopted in this study further contributes to the observed stability and consistency of the ECR-derived deformation time series. In particular, the reduced max_topo_err threshold limits the inclusion of spatially offset PS candidates caused by sidelobe effects around strong artificial reflectors. A dedicated methodological investigation demonstrated that relaxed topographic error thresholds can substantially increase apparent PS density around electronic corner reflectors, but at the expense of spatial ambiguity and increased phase noise, whereas stricter thresholds improve the robustness and interpretability of the resulting deformation signals [83]. In the context of operational dam monitoring, this quality-driven trade-off is considered preferable to maximizing point density.

Differences in PSI-derived displacements between ascending and descending geometries primarily result from the measurement geometry itself. PSI measures displacement in the radar line of sight, which differs between the two orbits in azimuth and incidence angle. As shown by Ziemer et al. [45], the projection of radial dam deformation into Sentinel-1 LOS typically reduces the observable displacement by a factor of approximately 0.3–0.6 for ascending tracks and 0.2–0.5 for descending tracks, depending on dam orientation and viewing geometry. These attenuation factors quantitatively illustrate that identical physical deformation can appear substantially different in the two orbits.

An identical 3D displacement vector is therefore projected differently onto the line of sight in each orbit: vertical components contribute similarly in both, whereas east–west motion components change sign and amplitude, and north–south components exhibit low sensitivity [71,85]. Additional azimuth- and angle-dependent effects, together with the specific orientation of each dam relative to the satellite heading, further modify how radial or lateral deformation projects into the LOS. Dams that are aligned more parallel or perpendicular to the LOS therefore show systematically different attenuation behavior, complicating direct orbit comparison.

In addition to geometric projection effects, orbit-dependent differences in deformation consistency are also influenced by atmospheric conditions. Ascending and descending Sentinel-1 acquisitions are performed at different local times, with descending passes typically occurring in the morning and ascending passes in the evening. Diurnal variations in temperature and humidity can lead to systematic differences in tropospheric delay, which may not be fully captured by standard APS estimation and can therefore affect deformation consistency between orbits, particularly at individual sites [74,75,84]. Such orbit-dependent atmospheric effects have been reported in previous InSAR studies and are known to introduce residual phase artifacts even in multi-temporal analyses [71].

Furthermore, local topographic and structural effects play an important role in dam environments. The geometry of dam bodies, adjacent slopes, and reservoir surfaces can cause orbit-specific shadowing, layover, and partial occlusion of radar targets, leading to variations in signal quality and phase stability between ascending and descending viewing geometries [76,77,86]. These effects are particularly pronounced for large or complex structures, where small changes in incidence angle and azimuth can substantially alter the effective radar illumination of the dam surface and the reliability of phase measurements. Similar geometry-driven differences between satellite tracks have been reported for infrastructure and terrain with strong relief, emphasizing that orbit-dependent discrepancies are an inherent characteristic of spaceborne InSAR observations [71,86].

When comparing PSI with plumb-line measurements, it must be noted that PSI observes LOS displacement, whereas the plumb line records radial deformation. These geometries are not equivalent: a positive LOS signal indicates motion toward the satellite and may only partially represent radial movements, depending on the dam orientation. Consequently, amplitude differences between PSI and plumb-line curves are expected. Ascending and descending tracks differ further in their projection of radial deformation into the LOS direction, which can cause one orbit to show better agreement than the other. A fully consistent comparison would require projecting the plumb-line measurements into the satellite line of sight or decomposing the PSI results into vertical and horizontal components. Such transformations were not applied in this study, as they would require additional assumptions on deformation direction and geometry that are not consistently available across all sites and measurement types. Instead, the comparison is intended to assess consistency, temporal behavior, and order of magnitude. Consequently, RMSE and correlation values should be interpreted with caution and in the context of these methodological constraints.

Additional radiometric effects can further modulate the ascending–descending differences. Although normalization to γ^0 and radiometric terrain correction reduce angle- and topography-related variability, residual azimuthal anisotropy and incidence-angle dependence are still known for Sentinel-1 [76–78]. Near-structure effects such as layover and multipath, which are pronounced at dams due to water surfaces and orthogonal walls, can additionally alter amplitude and phase in a geometry-dependent way. Given the high long-term radiometric stability of Sentinel-1 [87], persistent orbit-wise offsets are therefore best explained by geometry- and normalization-related factors rather than instrument drift.

Target- and instrument-related aspects also play a role: slight deviations from optimal ECR orientation, temperature-dependent amplification, timing or frequency stability, and transmission interruptions affect signal strength and phase noise, while sidelobes can generate additional PS points nearby [36–38,41,88,89]. Complementary studies on passive corner reflectors in complex terrain confirm the importance of geometry, reflector size, orientation, and site selection for achieving high RCS and robust signal-to-clutter ratios [28,90]. A joint evaluation of ascending and descending results, optionally constrained by

GNSS observations, allows decomposition into vertical and east–west components and thus enhances interpretability [86].

The representativeness of the validation is limited by the small number and non-colocation of trigonometric measurements, their low temporal frequency, and differing start and end dates of the time series. Over the 31-month observation period, the total number of trigonometric measurements remains in the single-digit range for some dams, limiting statistical significance.

A systematic offset is visible at several dams, where trigonometric measurements show larger deformation amplitudes than the PSI-derived values. This behavior is expected for several reasons: (i) trigonometric data capture horizontal displacement components directly, whereas PSI measures only the line-of-sight projection, which reduces amplitudes when deformation is not aligned with the LOS; (ii) local geometry at dam crests and abutments can amplify lateral movements that are only partially visible in PSI; (iii) differences in spatial sampling (point-based surveys versus distributed radar footprints) may lead to comparing non-identical structural elements; and (iv) the small number of trigonometric survey epochs increases statistical variability. These factors explain why in situ amplitudes tend to be higher than their PSI counterparts, even when seasonal patterns and relative trends match well. Accordingly, harmonization of measurement epochs, increased survey frequency, or a longer observation period would improve reliability.

The radial component of the trigonometric data captures only the horizontal component of deformation, while the vertical component is not included. However, at embankment dams, vertical movements often represent a major share of the total deformation [56–61]. Because deformation at embankment dams typically involves a site-specific combination of horizontal and vertical motion, direct comparison with the radial component of trigonometric measurements is therefore less conclusive than for gravity dams [56–61]. The comparison with plumb-line data at the Möhne Dam benefits from the high temporal resolution: daily sampling enables closer temporal coincidence with Sentinel-1 acquisitions, reduces aliasing effects, and increases the number of matching observations. In the present dataset, these factors lead to a somewhat more stable alignment of medium-term trends, although the resulting correlations remain moderate and therefore must be interpreted with caution [71].

For operational implementation, it is therefore essential to define minimum data requirements, such as sufficient scene density per year and orbit, maximum tolerable data gaps, and practical thresholds for alerting or notification [91].

For geodetic anchoring and reliable accuracy assessment, the co-location of passive CRs and GNSS stations is advisable, while potential GNSS multipath effects caused by nearby reflectors need to be considered [92,93]. For large-scale comparability and contextual evaluation, the EGMS framework provides a useful reference for applications and quality standards [94].

Field tests with active transponders and electronic reflectors have shown that compact active devices can produce stable time series over extended periods, although temperature dependence and occasional outages remain practical constraints [88,89]. Our results confirm these findings under operational dam conditions: all installed ECRs provided high and persistent backscatter levels, and PSI identified at least one coherent PS per reflector in both viewing geometries. Only isolated outages affected the temporal continuity at some sites.

Compared to passive CRs, which require careful sizing and alignment to ensure a sufficient radar cross section [28,90], the compact ECR design proved advantageous in the present dam studies, where access, safety, and visibility constraints limit the deployment of bulkier passive structures. In these settings, ECRs substantially improve the availability

of stable reference points on dam bodies and abutments, particularly where natural persistent scatterers are sparse.

To place these results in a broader context, the obtained accuracy metrics can be compared with benchmark values reported in the InSAR literature. For Sentinel-1, systematic comparisons with GNSS and precise leveling have been reported, indicating standard deviations of vertical velocity differences of about 9 to 10 mm/year relative to GNSS and approximately 8 mm/year relative to leveling data. A good agreement between PSI and Small Baseline Subset (SBAS) has also been demonstrated, with standard deviations of rate differences of about 6 mm/year (vertical) and 4 mm/year (east–west) [95,96]. In this study, the level of agreement between PSI-derived and in situ measurements falls within the range of error magnitudes commonly reported for Sentinel-1-based deformation monitoring. RMSE values of 2 to 5 mm for the trigonometric validation and 2 to 3 mm for the plumb-line comparison are consistent with these ranges when interpreted in the context of the known geometric and methodological limitations of the comparison.

Additional inter-comparisons and benchmarking studies show that Sentinel-1-based InSAR products, when processed consistently, achieve comparable accuracy levels, in some well-observed regions even reaching standard deviations of ≤2 to 3 mm/year [26,97], indicating that the ECR-based PSI results achieve accuracy levels consistent with, and in several cases approaching, those reported in benchmark studies.

For corner reflectors, several validation studies exist. Five-year CR time series have been used for quality control of the InSAR phase, demonstrating stable, millimeter-accurate temporal evolution [98]. Controlled experiments with artificially induced millimeter-scale displacements on dihedral reflectors confirmed that InSAR can reproducibly detect such displacements, achieving sub-millimeter precision under favorable conditions [99]. Active transponders and ECRs have been operating in field tests for more than a year, yielding consistent, cross-track Sentinel-1 time series that confirm their suitability as stable reference targets for geodetic InSAR applications [88]. Studies on the joint use of CRs and geodetic benchmarks highlight that co-locating CRs with GNSS stations facilitates the assessment of accuracy and integration into a stable reference frame [99]. These findings are consistent with recent work demonstrating the successful deployment of ECRs in dam environments, confirming both their high signal stability and their operational feasibility [44].

Temperature sensitivity represents a potential limitation of electronic corner reflectors, particularly over long observation periods and under pronounced seasonal variations. In the present study, temperature-induced phase variations are not explicitly corrected, but their impact is implicitly reduced through multi-temporal PSI processing and the use of network-based phase estimation. The good agreement between ECR-derived deformation time series and independent plumb and trigonometric measurements suggests that residual temperature effects do not dominate the observed deformation signals at the investigated sites. Nevertheless, dedicated temperature compensation strategies may further improve robustness in environments with extreme thermal conditions.

In summary, these results emphasize that ECR-based PSI can achieve accuracy levels comparable to established geodetic techniques when supported by consistent processing, adequate temporal coverage, and proper installation design. This positions ECRs as a reliable and practical extension of conventional monitoring networks for long-term, satellite-based infrastructure surveillance. At the same time, maintenance and power supply requirements represent practical limitations that must be considered in operational deployments. Under suitable logistical conditions, however, ECRs can extend PSI applicability to locations where passive reflectors are not feasible.

5.3. Advantages of the (On-Demand) Web Service

The presented web service constitutes the concluding element of a comprehensive investigation concept that complements DIN-compliant monitoring programs for dams and other critical infrastructures. Rather than replacing established, norm-based instrumentation, it augments routine practice with standardized satellite-based PSI products, including CR Index and PS measurements based on ECRs, delivered in a consistent and operator-focused workflow.

Compared to broad, centralized platforms (e.g., BBD, EGMS) [5–7], the service follows a local, asset-level approach. Operators retain data sovereignty, can integrate their own datasets, and generate timely PSI updates. Interactive time-series plots, direct comparison of multiple PS points (including basic statistics), polygon-based bulk export, and shareable map states support day-to-day assessments and reporting. For the Ruhrverband, seamless handover is ensured via one-click downloads in a Ruhrverband-compatible format and optional scheduled conversions, enabling smooth integration into existing environments with minimal overhead. This functionality can be easily extended to other operators.

The representation is scientifically conservative by default: Line-of-Sight remains the primary visualization in line with recent findings, while motion-decomposed products (e.g., radial, vertical, horizontal) will be offered in upcoming updates of the application, only where they add demonstrable value and are clearly labeled. Additional motion-decomposed or derived layers can be brought in via Python-based ingestion and conversion scripts, which also validate inputs, update the data index, and standardize presentation.

Software architecture yields an extensible solution that other dam operators or operators of critical infrastructure can adopt rapidly, by adding new areas, sources, or export profiles, while keeping outputs reproducible and compatible with existing, DIN-aligned monitoring programs. In summary, the service operationalizes PSI (including CR Index [44] and PSI-ECR) as a maintainable, operator-centric complement to established measurement regimes.

A public release of the software is planned in a later project phase. The current prototype cannot be published because it contains integrated in situ measurements from the Ruhrverband, which constitute sensitive operational data. A dedicated release version will therefore be prepared that excludes these datasets and provides a generalized ingestion interface, allowing dam operators to integrate their own monitoring data into the system. This will facilitate the transfer of the presented workflow to additional infrastructure operators.

6. Conclusions

This study extends previous research on satellite-based dam monitoring by establishing a comprehensive and operational monitoring concept for dam infrastructure. The ECR installations proved to be technically feasible and delivered stable, interpretable time series that could be directly compared with in situ data. The analyses demonstrated that ECRs provide stable, high-quality reference points in scatterer-poor dam environments, thereby ensuring reliable PSI measurements where natural persistent scatterers are limited and thus provide an effective means of integrating artificial reference points into routine monitoring workflows. Specifically, all six installed ECRs exhibited consistently low Amplitude Dispersion Index values (ADI ≤ 0.4) over observation periods of up to 31 months, confirming their suitability as stable radar targets for multi-year C-band PSI. The internal consistency of deformation time series across two processing windows (24 and 31 months) was high, with correlations exceeding 0.9 and RMSE values typically below 0.5 mm at most sites, demonstrating the reproducibility of the ECR-derived deformation signals under operational conditions.

A quantitative accuracy assessment confirms that the achieved precision of the ECR-based PSI measurements is within the performance range expected for Sentinel 1 deformation monitoring. Validation against trigonometric measurements yields Root Mean Square Error values of typically 2 to 5 mm, while comparisons with plumb line data show RMSE values of approximately 2 to 3 mm. These accuracy levels align with published benchmarks for Sentinel 1-based InSAR analyses and confirm that the proposed monitoring concept provides deformation estimates consistent with established geodetic techniques.

Beyond the hardware perspective, the project outcomes were consolidated in a web-based service that makes all processed PSI results, including ECR-based time series, available to dam operators. This service provides user-friendly access to interactive time series, displacement maps, and supplementary indices, thereby facilitating the interpretation of complex InSAR products for practical decision making. By combining multiyear PSI analyses, engineered reflectors, and a dedicated web platform, the presented workflow represents a comprehensive monitoring framework tailored to the needs of dam safety management. To our knowledge, this constitutes the first operational PSI service integrating ECR-based deformation time series with site-specific web visualization and standardized download capabilities designed for dam operators. The service complements existing large-scale ground motion products such as BBD and EGMS by providing site-specific analyses at ECR locations that are not covered by national-scale platforms.

The findings underline the relevance of remote sensing as a complementary tool for infrastructure surveillance. The developed methodology not only supports dam operators in NRW, Germany, but also provides a transferable foundation for other operators and water authorities worldwide. In light of climate-driven stressors such as prolonged droughts and extreme precipitation, reliable monitoring strategies will gain further importance. The present study demonstrates that the integration of ECR-supported PSI into operational workflows is technically feasible, produces deformation estimates consistent with in situ geodetic techniques, and can be delivered through accessible, operator-oriented platforms. These results provide a concrete and quantitatively validated basis for the broader adoption of Earth Observation in dam safety management.

Author Contributions: Conceptualization, J.J., J.Z. and C.D.; methodology, J.J. and J.Z.; software, J.J., J.Z. and L.S.; validation, J.J., J.Z., C.W., K.L., C.S. and C.D.; formal analysis, J.J., J.Z., C.W. and C.D.; investigation, J.J. and J.Z.; resources, J.J., J.Z., C.W. and L.S.; data curation, J.J. and J.Z.; writing—original draft preparation, J.J.; writing—review and editing, J.J., J.Z., C.W., C.S., C.D., L.S. and J.B.; visualization, J.J. and J.Z.; supervision, K.L., C.S., C.D. and J.B.; project administration, C.S. and C.D.; funding acquisition, K.L., C.S. and C.D. All authors have read and agreed to the published version of the manuscript.

Funding: This research was funded by DLR with funds provided by the Federal Ministry for Economic Affairs and Climate Action (BMWK) due to an enactment of the German Bundestag, grant number 50EE2202A. We also acknowledge support by the German Research Foundation Projekt-Nr. 512648189, and the Open Access Publication Fund of the Thüringer Universitäts- und Landesbibliothek Jena.

Data Availability Statement: The data presented in this study are available on request from the corresponding author. The data are not publicly available due to legal and privacy issues.

Conflicts of Interest: The authors declare no conflicts of interest.

Abbreviations

The following abbreviations are used in this manuscript:

ADI	Amplitude Dispersion Index
APS	Atmospheric Phase Screen
BBD	BodenbewegungsDienst Deutschland—German Ground Motion Service
DEM	Digital Elevation Model
DIN	Deutsches Institut für Normung—German Institute for Standardization
DInSAR	Differential Interferometric SAR
ECR	Electronic Corner Reflector
EGMS	European Ground Motion Service
ESA	European Space Agency
ESD	Enhanced Spectral Diversity
GDI	Geodata Infrastructure
GMS	Ground Motion Service
GNSS	Global Navigation Satellite System
IW	Interferometric Wide Swath
LOS	Line-of-Sight
LUI	Land-Use Index
MAE	Mean Absolute Error
MedAE	Median Absolute Error
MT-InSAR	Multi-Temporal Interferometric Synthetic Aperture Radar
PS	Persistent Scatterer Pixel
PSI	Persistent Scatterer Interferometry
RCS	Radar Cross Section
RMSE	Root Mean Square Error
SAR	Synthetic Aperture Radar
SBAS	Small Baseline Subset
SLC	Single-Look-Complex
SNAP	Sentinel Application Platform
StaMPS	Stanford Method for Persistent Scatterers
TOPS	Terrain Observation with Progressive Scans

Appendix A

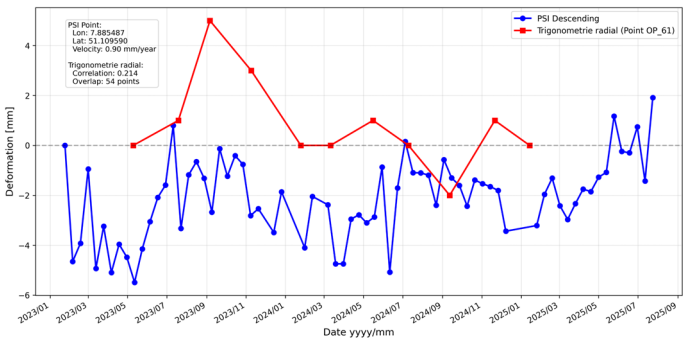

(**A**)

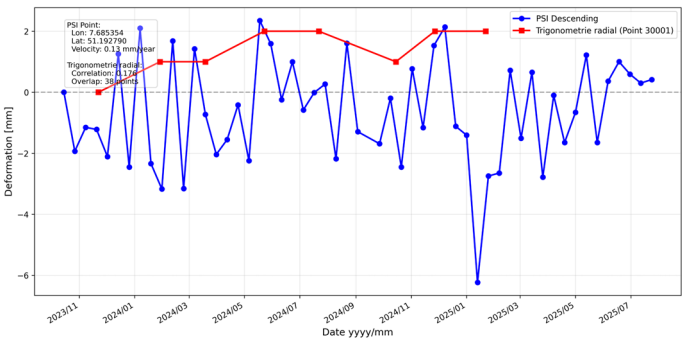

(**D**)

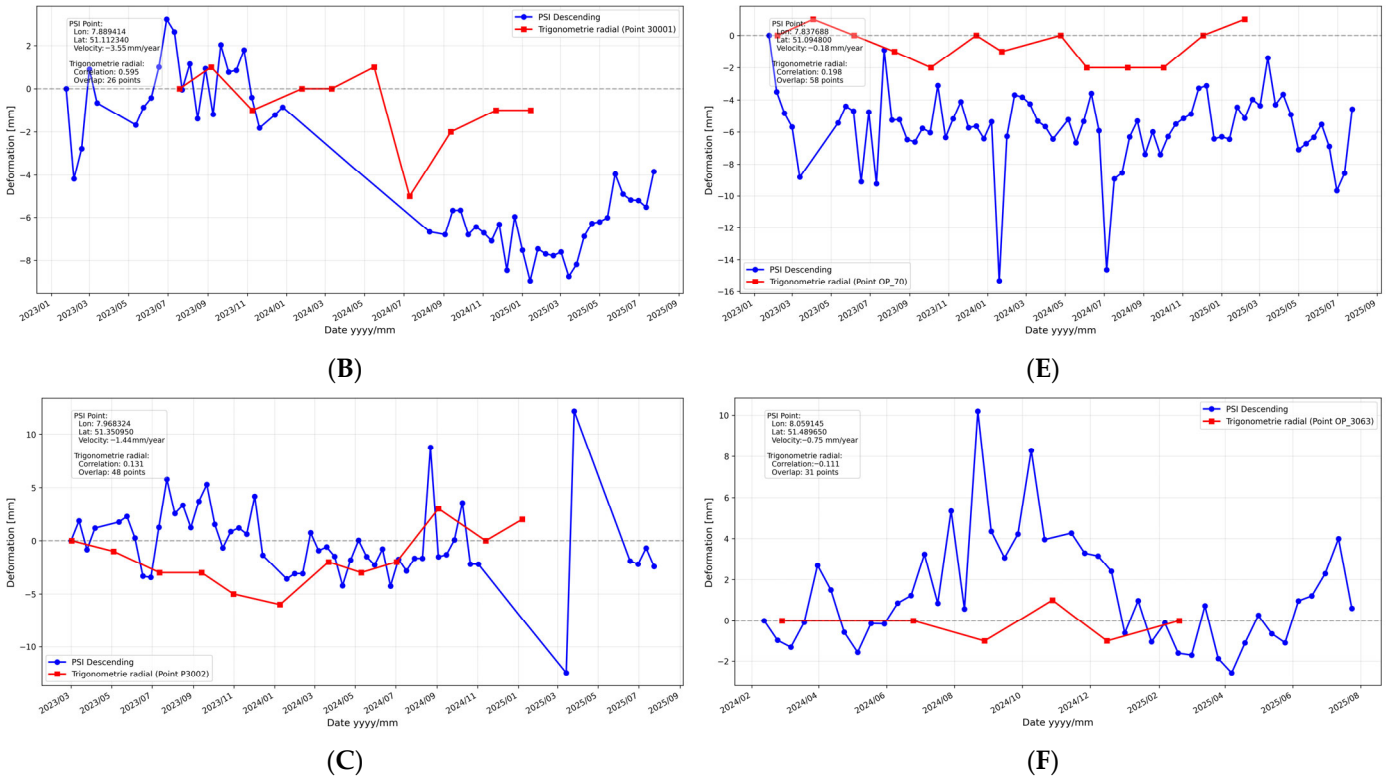

Figure A1. Descending-track LOS deformation of the analyzed ECRs, statistically validated against trigonometric measurements; summary statistics of agreement are included. (**A**) Bigge 1; (**B**) Bigge 2; (**C**) Sorpe; (**D**) Verse; (**E**) Lister; (**F**) Möhne.

References

1. Jänichen, J.; Schmullius, C.; Baade, J.; Last, K.; Bettzieche, V.; Dubois, C. Monitoring of Radial Deformations of a Gravity Dam Using Sentinel-1 Persistent Scatterer Interferometry. *Remote Sens.* **2022**, *14*, 1112. https://doi.org/10.3390/rs14051112.
2. Bettzieche, V. Satellitenüberwachung der Verformungen von Staumauern und Staudämmen. *WasserWirtschaft* **2020**, *110*, 48–51. https://doi.org/10.1007/s35147-020-0424-9.
3. Ferretti, A.; Prati, C.; Rocca, F. Analysis of Permanent Scatterers in SAR Interferometry. In *IGARSS 2000—IEEE International Geoscience and Remote Sensing Symposium, Proceedings, Honolulu, HI, USA, 24–28 July 2000*; IEEE: Piscataway, NJ, USA, 2000; Volume 2, pp. 761–763. https://doi.org/10.1109/IGARSS.2000.861695.
4. Ferretti, A.; Prati, C.; Rocca, F. Permanent Scatterers in SAR Interferometry. *IEEE Trans. Geosci. Remote Sens.* **2001**, *39*, 8–20. https://doi.org/10.1109/36.898661.
5. Kalia, A.C.; Frei, M.; Lege, T. BodenBewegungsdienst Deutschland (BBD): Konzept, Umsetzung und Service-Plattform. *zfv—Zeitschrift für Geodäsie Geoinformation und Landmanagement* **2021**, *146*, 273–279. https://doi.org/10.12902/zfv-0365-2021.
6. Bundesanstalt für Geowissenschaften und Rohstoffe (BGR). BodenBewegungsdienst Deutschland (BBD) Web App. Available online: https://bodenbewegungsdienst.bgr.de/mapapps/resources/apps/bbd/index.html?lang=de (accessed on 15 August 2025).
7. Copernicus Land Monitoring Service. European Ground Motion Service (EGMS)—Product Overview. Available online: https://land.copernicus.eu/en/products/european-ground-motion-service (accessed on 15 August 2025).
8. Even, M.; Westerhaus, M.; Kutterer, H. German and European Ground Motion Service: A Comparison. *PFG—J. Photogramm. Remote Sens. Geoinf. Sci.* **2024**, *92*, 253–270. https://doi.org/10.1007/s41064-024-00273-3.
9. Hrysiewicz, A.; Khoshlahjeh Azar, M.; Holohan, E.P. EGMS-toolkit: A Set of Python Scripts for Improved Access to Datasets from the European Ground Motion Service. *Earth Sci. Inform.* **2024**, *17*, 3825–3837. https://doi.org/10.1007/s12145-024-01356-w.
10. Jänichen, J.; Ziemer, J.; Wicker, C.; Last, K.; Schmullius, C.; Kalia, A.C.; Lege, T.; Dubois, C. Evaluating the German Ground Motion Service for Operational Dam Monitoring: A Comparison of InSAR Data with In Situ Measurements. *Remote Sens.* **2025**, *17*, 3649. https://doi.org/10.3390/rs17213649.
11. Milillo, P.; Porcu, M.C.; Lundgren, P.; Soccodato, F.; Salzer, J.; Fielding, E.; Bürgmann, R.; Milillo, G.; Perissin, D.; Biondi, F. The ongoing destabilization of the Mosul Dam as observed by synthetic aperture radar interferometry. In *Proceedings of IGARSS*

2017—IEEE International Geoscience and Remote Sensing Symposium, Fort Worth, TX, USA, 23–28 July 2017; IEEE: Piscataway, NJ, USA, 2017; pp. 6279–6282. https://doi.org/10.1109/IGARSS.2017.8128442.

12. Ruiz-Armenteros, A.M.; Lazecky, M.; Hlaváčová, I.; Bakoň, M.; Delgado, J.M.; Sousa, J.J.; Lamas-Fernández, F.; Marchamalo, M.; Caro-Cuenca, M.; Papco, J.; et al. Deformation monitoring of dam infrastructures via spaceborne MT-InSAR. The case of La Viñuela (Málaga, southern Spain). *Procedia Comput. Sci.* **2018**, *138*, 346–353. https://doi.org/10.1016/j.procs.2018.10.049.
13. Abo, H.; Osawa, T.; Ge, P.; Takahashi, A.; Yamagishi, K. Deformation Monitoring of Large-Scale Rockfill Dam Applying Persistent Scatterer Interferometry (PSI) Using Sentinel-1 SAR Data. In *Proceedings of APSAR 2021—7th Asia-Pacific Conference on Synthetic Aperture Radar, Bali, Indonesia, 1–3 November 2021*; IEEE: Piscataway, NJ, USA, 2021; pp. 1–6. https://doi.org/10.1109/APSAR52370.2021.9688461.
14. Corsetti, M.; Fossati, F.; Manunta, M.; Marsella, M. Advanced SBAS-DInSAR technique for controlling large civil infrastructures: An application to the Genzano di Lucania dam. *Sensors* **2018**, *18*, 2371. https://doi.org/10.3390/s18072371.
15. Othman, A.A.; Al-Maamar, A.F.; Al-Manmi, D.A.M.; Liesenberg, V.; Hasan, S.E.; Al-Saady, Y.I.; Shihab, A.T.; Khwedim, K. Application of DInSAR-PSI technology for deformation monitoring of the Mosul Dam, Iraq. *Remote Sensing* **2019**, *11*, 2632. https://doi.org/10.3390/rs11222632.
16. Bayik, C.; Abdikan, S.; Arıkan, M. Long term displacement observation of the Atatürk Dam, Turkey by multi-temporal InSAR analysis. *Acta Astronaut.* **2021**, *189*, 483–491. https://doi.org/10.1016/j.actaastro.2021.09.022.
17. Marchamalo-Sacristán, M.; Ruiz-Armenteros, A.M.; Lamas-Fernández, F.; González-Rodrigo, B.; Martínez-Marín, R.; Delgado-Blasco, J.M.; Bakon, M.; Lazecky, M.; Perissin, D.; Papco, J.; et al. MT-InSAR and dam modeling for the comprehensive monitoring of an Earth-fill dam: The case of the Benínar dam (Almería, Spain). *Remote Sens.* **2023**, *15*, 2802. https://doi.org/10.3390/rs15112802.
18. Marchamalo-Sacristán, M.; Fernández-Landa, A.; Sancho, C.; Hernández-Cabezudo, A.; Krishnakumar, V.; García-Lanchares, C.; Sánchez, J.; Rubén, M.M.; Rejas-Ayuga, J.; González-Tejada, I.; et al. EyeRADAR-Dam: Integration of MT-InSAR with monitoring technologies in a pilot monitoring system for embankment dams. *Procedia Comput. Sci.* **2024**, *239*, 2286–2292. https://doi.org/10.1016/j.procs.2024.06.420.
19. Wang, Z.; Perissin, D. Cosmo-SkyMed AO projects—3D reconstruction and stability monitoring of the Three Gorges Dam. In *Proceedings of IGARSS 2012—IEEE International Geoscience and Remote Sensing Symposium, Munich, Germany, 22–27 July 2012*; IEEE: Piscataway, NJ, USA, 2012; pp. 3831–3834. https://doi.org/10.1109/IGARSS.2012.6350577.
20. Lazecky, M.; Perissin, D.; Lei, L.; Qin, Y.; Scaioni, M. Plover Cove Dam Monitoring with Spaceborne InSAR Technique in Hong Kong. In Proceedings of the 2nd Joint International Symposium on Deformation Monitoring (JISDM), Nottingham, UK, 9–10 September 2013; pp. 9–11. Available online: http://www.sarproz.com/wp-content/papercite-data/pdf/lazecky-pcdmwsitihk2013.pdf (accessed on 21 August 2025).
21. Tomás, R.; Cano, M.; Garcia-Barba, J.; Vicente, F.; Herrera, G.; Lopez-Sanchez, J.M.; Mallorquí, J. Monitoring an earthfill dam using differential SAR interferometry: La Pedrera dam, Alicante, Spain. *Eng. Geol.* **2013**, *157*, 21–32. https://doi.org/10.1016/j.enggeo.2013.01.022.
22. Dubois, C.; Ziemer, J.; Jänichen, J.; Stumpf, N.; Liedel, C.; Sabrowski, M.; Schmullius, C. Dam Monitoring With Ground Motion Services—A Case Study of a Gravity Dam with the German Ground Motion Service. In *Proceedings of IGARSS 2024—IEEE International Geoscience and Remote Sensing Symposium, Athens, Greece, 7–12 July 2024*; IEEE: Piscataway, NJ, USA, 2024; pp. 4670–4673. https://doi.org/10.1109/IGARSS53475.2024.10641662.
23. Stein, G.; Ziemer, J.; Wicker, C.; Jänichen, J.; Demisch, G.; Klöpper, D.; Last, K.; Denzler, J.; Schmullius, C.; Shadaydeh, M.; et al. Data-Driven Prediction of Large Infrastructure Movements Through Persistent Scatterer Time Series Modeling. In *Proceedings of IGARSS 2024—IEEE International Geoscience and Remote Sensing Symposium, Athens, Greece, 7–12 July 2024*; IEEE: Piscataway, NJ, USA, 2024; pp. 8669–8673. https://doi.org/10.1109/IGARSS53475.2024.10642253.
24. Garthwaite, M.C. On the Design of Radar Corner Reflectors for Deformation Monitoring in Multi-Frequency InSAR. *Remote Sens.* **2017**, *9*, 648. https://doi.org/10.3390/rs9070648.
25. Qin, Y.; Perissin, D.; Lei, L. The Design and Experiments on Corner Reflectors for Urban Ground Deformation Monitoring in Hong Kong. *Int. J. Antennas Propag.* **2013**, *2013*, 191685. https://doi.org/10.1155/2013/191685.
26. Marinković, P.; Ketelaar, V.B.H.; van Leijen, F.J.; Hanssen, R.F. InSAR Quality Control: Analysis of Five Years of Corner Reflector Time Series. In *Proceedings of the Fifth International Workshop on ERS/Envisat SAR Interferometry (FRINGE07), Frascati, Italy, 26–30 November 2007*; Lacoste, H., Ouwehand, L., Eds.; ESA SP-649; ESA Communications: Noordwijk, The Netherlands, 2008; pp. 1–8.

27. Kotulak, N.; Mleczko, M.; Crosetto, M.; Palamà, R.; Mróz, M. Interferometric SAR Deformation Monitoring Using Passive Reflectors and Ascending and Descending Passes. *Int. Arch. Photogramm. Remote Sens. Spatial Inf. Sci.* **2022**, *XLIII-B3-2022*, 285–292. https://doi.org/10.5194/isprs-archives-XLIII-B3-2022-285-2022.
28. Jauvin, M.; Yan, Y.; Trouvé, E.; Fruneau, B.; Gay, M.; Girard, B. Integration of Corner Reflectors for the Monitoring of Mountain Glacier Areas with Sentinel-1 Time Series. *Remote Sens.* **2019**, *11*, 988. https://doi.org/10.3390/rs11080988.
29. Czikhardt, R.; van der Marel, H.; Papco, J. GECORIS: An Open-Source Toolbox for Analyzing Time Series of Corner Reflectors in InSAR Geodesy. *Remote Sens.* **2021**, *13*, 926. https://doi.org/10.3390/rs13050926.
30. Dheenathayalan, P.; Caro Cuenca, M.; Hoogeboom, P.; Hanssen, R.F. Small Reflectors for Ground Motion Monitoring with InSAR. *IEEE Trans. Geosci. Remote Sens.* **2017**, *55*, 6703–6712. https://doi.org/10.1109/TGRS.2017.2731424.
31. Strozzi, T.; Teatini, P.; Tosi, L.; Wegmüller, U.; Werner, C. Land Subsidence of Natural Transitional Environments by Satellite Radar Interferometry on Artificial Reflectors. *J. Geophys. Res. Earth Surf.* **2013**, *118*, 1177–1191. https://doi.org/10.1002/jgrf.20082.
32. Qin, Y.; Perissin, D. Monitoring Ground Subsidence in Hong Kong via Spaceborne Radar: Experiments and Validation. *Remote Sens.* **2015**, *7*, 10715–10736. https://doi.org/10.3390/rs70810715.
33. Hasni, K.; Gourine, B.; Larabi, M.E.A. Dam Deformation Monitoring using Cloud-Based P-SBAS Algorithm: The Kramis Dam Case (Algeria). *Eng. Technol. Appl. Sci. Res.* **2023**, *13*, 10759–10764. https://doi.org/10.48084/etasr.5857.
34. Gourine, B.; Hasni, K. First Algerian Experiment of Manufactured Corner Reflectors for an Embankment Dam Monitoring: Case of Kramis Dam (Mostaganem, Algeria). In Proceedings of the World Multidisciplinary Earth Sciences Symposium (WMES 2019), Prague, Czech Republic, 9–13 September 2019.
35. Gourine, B.; Hasni, K.; Allal, S.H. Deformation Monitoring of Kramis's Dam Region (State of Mostaganem, Algeria) by Radar Interferometry Using SBAS Technique: First Results. In Proceedings of FRINGE 2021—11th International Workshop on Advances in the Science and Applications of SAR Interferometry, Amsterdam, The Netherlands, 31 May–4 June 2021.
36. Mahapatra, P.S.; Samiei-Esfahany, S.; Hanssen, R.F. Performance Evaluation of Advanced Corner Reflector Designs for InSAR Applications. *Remote Sens.* **2023**, *15*, 2789. https://doi.org/10.3390/rs15112789.
37. Balss, U.; Eineder, M.; Suchandt, S.; Gisinger, C. Compact Polyhedral Corner Reflectors for Sentinel-1 InSAR Applications. *Remote Sens. Environ.* **2022**, *268*, 112776. https://doi.org/10.1016/j.rse.2021.112776.
38. van der Marel, H.; van Leijen, F.J.; Hanssen, R.F. First Analysis of C-Band ECR Transponders for InSAR Geodesy. In *IGARSS 2018—IEEE International Geoscience and Remote Sensing Symposium; Valencia, Spain, 22–27 July 2018*; IEEE: Piscataway, NJ, USA, 2018; pp. 1399–1402. https://doi.org/10.1109/IGARSS.2018.8518924.
39. Gisinger, C.; Eineder, M.; Brcic, R.; Balss, U.; Gruber, T.; Oikonomidou, X.; Heinze, M. First Experiences with Active C-Band Radar Reflectors and Sentinel-1. In *Proceedings of the IGARSS 2020—IEEE International Geoscience and Remote Sensing Symposium, Waikoloa, HI, USA, 26 September–2 October 2020*; IEEE: Piscataway, NJ, USA, 2020; pp. 6356–6359. https://doi.org/10.1109/IGARSS39084.2020.9324381.
40. Luzi, G.; Espín-López, P.F.; Mira Pérez, F.; Monserrat, O.; Crosetto, M. A Low-Cost Active Reflector for Interferometric Monitoring Based on Sentinel-1 SAR Images. *Sensors* **2021**, *21*, 2008. https://doi.org/10.3390/s21062008.
41. MetaSensing B.V. ECR-C Electronic Corner Reflector (Datasheet). 2022. Available online: https://metasensing.com/wp-content/uploads/2022/07/MetaSensing-ecr-c.pdf (accessed on 15 August 2025).
42. Fotiou, K.; Danezis, C. An Overview of Electronic Corner Reflectors and Their Use in Ground Deformation Monitoring Applications. In *Proceedings of the Eighth International Conference on Remote Sensing and Geoinformation of the Environment (RSCy2020), Paphos, Cyprus, 26–29 August 2020*; Proc. SPIE; SPIE: Bellingham, WA, USA, 2020; Volume 11524, p. 115240N. https://doi.org/10.1117/12.2571886.
43. Mahapatra, P.S.; Samiei-Esfahany, S.; van der Marel, H.; Hanssen, R.F. On the Use of Transponders as Coherent Radar Targets for SAR Interferometry. *IEEE Trans. Geosci. Remote Sens.* **2014**, *52*, 1859–1878. https://doi.org/10.1109/TGRS.2013.2255881.
44. Jänichen, J.; Ziemer, J.; Wolsza, M.; Klöpper, D.; Weltmann, S.; Wicker, C.; Last, K.; Schmullius, C.; Dubois, C. Towards Operational Dam Monitoring with PS-InSAR and Electronic Corner Reflectors. *Remote Sens.* **2025**, *17*, 1318. https://doi.org/10.3390/rs17071318.
45. Ziemer, J.; Jänichen, J.; Wicker, C.; Klöpper, D.; Last, K.; Kalia, A.; Lege, T.; Schmullius, C.; Dubois, C. Assessing the Feasibility of Persistent Scatterer Data for Operational Dam Monitoring in Germany: A Case Study. *Remote Sens.* **2025**, *17*, 1202. https://doi.org/10.3390/rs17071202.
46. Ziemer, J.; Stein, G.; Wicker, C.; Jänichen, J.; Klöpper, D.; Last, K.; Denzler, J.; Schmullius, C.; Shadaydeh, M.; Dubois, C. Enhancing the Prediction of Dam Deformations: A Novel Data-Driven Approach. *Remote Sens.* **2025**, *17*, 1026. https://doi.org/10.3390/rs17061026.

47. Bezirksregierung Köln, Geobasis NRW. Bodenbewegungskataster NRW. Available online: https://www.bezreg-koeln.nrw.de/geobasis-nrw/produkte-und-dienste/bodenbewegungen/bodenbewegungskataster-nrw (accessed on 15 November 2025).
48. Ruhrverband. Catchment of the river Ruhr and jurisdiction of the Ruhrverband. Available online: https://ruhrverband.de/flussgebiet/ (accessed on 14 April 2026).
49. OpenStreetMap Contributors. Geometrische Daten der Bundesländer Deutschlands. Data Derived from OpenStreetMap and Licensed Under the Open Database License (ODbL). Available online: https://openstreetmap.org (accessed on 20 April 2022).
50. Ruhrverband. Management of Water Resources in North Rhine-Westphalia. Available online: https://www.ruhrverband.de/ (accessed on 2 January 2026).
51. Geodata Infrastructure North Rhine-Westphalia (GDI-NRW). 3D-Messdaten Laserscanning—Paketierung: Einzelkacheln. Available online: https://www.opengeodata.nrw.de/produkte/geobasis/hm/3dm_l_las/3dm_l_las/ (accessed on 21 August 2025).
52. European Space Agency (ESA). Sentinel-1 Data Products. Available online: https://sentinel.esa.int/web/sentinel/missions/sentinel-1 (accessed on 14 April 2026).
53. Ruhrverband (Essen, Germany). (Möhnetalsperre, Möhnesee, Germany); Sicherheitsbericht 2013, Teil A. Unpublished security report, 2013.
54. Ruhrverband (Essen, Germany). (Möhnetalsperre, Möhnesee, Germany); Sicherheitsbericht 2020, Teil B. Unpublished security report, 2020.
55. Ruhrverband (Essen, Germany). (Möhnetalsperre, Möhnesee, Germany); Vertiefte Überprüfung 2018. Analyse der Messdaten. Unpublished security report, 2018.
56. Ruhrverband (Essen, Germany). (Versetalsperre, Lüdenscheid, Germany); Sicherheitsbericht 2020, Teil A. Unpublished security report, 2020.
57. Ruhrverband (Essen, Germany). (Versetalsperre, Lüdenscheid, Germany); Sicherheitsbericht 2020, Teil B. Unpublished security report, 2020.
58. Ruhrverband (Essen, Germany). (Biggetalsperre, Attendorn, Germany); Sicherheitsbericht 2019, Teil A. Unpublished security report, 2019.
59. Ruhrverband (Essen, Germany). (Biggetalsperre, Attendorn, Germany); Sicherheitsbericht 2020, Teil B. Unpublished security report, 2020.
60. Ruhrverband (Essen, Germany). (Sorpetalsperre, Sundern, Germany); Sicherheitsbericht 1993, Teil A. Unpublished security report, 1993.
61. Ruhrverband (Essen, Germany). (Sorpetalsperre, Sundern, Germany); Sicherheitsbericht 2020, Teil B. Unpublished security report, 2020.
62. Ziemer, J.; Jänichen, J.; Wicker, C.; Last, K.; Schmullius, C.; Dubois, C. First Assessment of Electronic Corner Reflectors for Dam Monitoring in Germany—A Case Study. In *Presented at the ESA Living Planet Symposium 2025 (LPS25), Vienna, Austria, 23–27 June 2025; Poster, Session B.04.05, 24 June 2025*; European Space Agency: Paris, France, 2025. Available online: https://lps25.esa.int/programme/programme-session/?id=A3FC4D29-9678-4261-8931-2D9A08647661&presentationId=FFCB7401-315A-4A70-8076-D2B371847B66 (accessed on 21 August 2025).
63. Mandal, D.; Vaka, D.S.; Bhogapurapu, N.R.; Vanama, V.S.K.; Kumar, V.; Rao, Y.S.; Bhattacharya, A. Sentinel-1 SLC Preprocessing Workflow for Polarimetric Applications: A Generic Practice for Generating Dual-pol Covariance Matrix Elements in SNAP S-1 Toolbox. *Preprints* **2019**. https://doi.org/10.20944/preprints201911.0393.v1.
64. Mancini, F.; Grassi, F. A Workflow Based on SNAP–StaMPS Open-Source Tools and GNSS Data for PSI-Based Ground Deformation Using Dual-Orbit Sentinel-1 Data: Accuracy Assessment with Error Propagation Analysis. *Remote Sens.* **2021**, *13*, 753. https://doi.org/10.3390/rs13040753.
65. Foumelis, M.; Delgado Blasco, J.M.; Desnos, Y.-L.; Engdahl, M.; Fernández, D.; Veci, L.; Lu, J.; Wong, C. ESA SNAP-StaMPS Integrated Processing for Sentinel-1 Persistent Scatterer Interferometry. In *Proceedings of IGARSS 2018–IEEE International Geoscience and Remote Sensing Symposium, Valencia, Spain, 22–27 July 2018*; IEEE: Piscataway, NJ, USA, 2018; pp. 1364–1367. https://doi.org/10.1109/IGARSS.2018.8519545.
66. Delgado Blasco, J.M.; Ziemer, J.; Foumelis, M.; Dubois, C.; SNAP2StaMPS v2: Increasing Features and Supported Sensors in the Open Source SNAP2StaMPS Processing Scheme. Zenodo. 2023. Available online: https://doi.org/10.5281/zenodo.8362628 (accessed on 14 April 2026).

67. Hooper, A.; Bekaert, D.; Hussain, E.; Spaans, K. *StaMPS/MTI Manual Manual, Version 4.1b*; University of Leeds: Leeds, UK, 2018. Available online: https://homepages.see.leeds.ac.uk/~earahoo/stamps/StaMPS_Manual_v4.1b1.pdf (accessed on 21 August 2025).
68. Serco Italia SPA. *StaMPS: Persistent Scatterer Interferometry Processing—Mexico City 2021, Version 1.1*; RUS Copernicus Training Kit HAZA12; ESA/RUS Copernicus: Frascati, Italy, 2021. Available online: https://eo4society.esa.int/wp-content/uploads/2022/01/HAZA12_StaMPsPSI_Processing_Tutorial.pdf (accessed on 1 April 2026).
69. Hooper, A.; Segall, P.; Zebker, H. Persistent Scatterer Interferometric Synthetic Aperture Radar for Crustal Deformation Analysis, with Application to Volcán Alcedo, Galápagos. *J. Geophys. Res. Solid Earth* **2007**, *112*, B07407. https://doi.org/10.1029/2006JB004763.
70. Hooper, A. A multi-temporal InSAR method incorporating both persistent scatterer and small baseline approaches. *Geophys. Res. Lett.* **2008**, *35*, L16302. https://doi.org/10.1029/2008GL034654.
71. Hooper, A.; Bekaert, D.; Spaans, K.; Arikan, M. Recent Advances in SAR Interferometry Time Series Analysis for Measuring Crustal Deformation. *Tectonophysics* **2012**, *514–517*, 1–13. https://doi.org/10.1016/j.tecto.2011.10.013.
72. Agafonkin, V. Leaflet—An Open-Source JavaScript Library for Interactive Maps. 2010. Available online: https://leafletjs.com (accessed on 21 August 2025).
73. *DIN 19700-10*; Dam Structures—Part 10: General Provisions. DIN: Berlin, Germany, 2004.
74. Brisco, B.; Brown, R.J.; Koehler, J.A.; Sofko, G.J.; McKibben, M.J. The diurnal pattern of microwave backscattering by wheat. *Remote Sens. Environ.* **1990**, *34*, 37–47. https://doi.org/10.1016/0034-4257(90)90082-W.
75. Karmakar, P.K.; Sengupta, L.; Maiti, M.; Angelis, C.F. Some of the atmospheric influences on microwave propagation through atmosphere. *Am. J. Sci. Res.* **2010**, *1*, 350–358. https://doi.org/10.5251/ajsir.2010.1.2.350.358.
76. Schaufler, S.; Bauer-Marschallinger, B.; Hochstöger, S.; Wagner, W. Modelling and correcting azimuthal anisotropy in Sentinel-1 backscatter data. *Remote Sens. Lett.* **2018**, *9*, 799–808. https://doi.org/10.1080/2150704X.2018.1480071.
77. Arias, M.; Campo-Bescós, M.Á.; Álvarez-Mozos, J. On the influence of acquisition geometry in backscatter time series over wheat. *Int. J. Appl. Earth Obs. Geoinf.* **2022**, *106*, 102671. https://doi.org/10.1016/j.jag.2021.102671.
78. Small, D. Flattening Gamma: Radiometric Terrain Correction for SAR Imagery. *IEEE Trans. Geosci. Remote Sens.* **2011**, *49*, 3081–3093. https://doi.org/10.1109/TGRS.2011.2120616.
79. El Hajj, M.; Baghdadi, N.; Zribi, M.; Bazzi, H. Analysis of Sentinel-1 Radiometric Stability and Quality for Land Surface Applications. *Remote Sens.* **2016**, *8*, 406. https://doi.org/10.3390/rs8050406.
80. Schmidt, K.; Schwerdt, M.; Miranda, N.; Reimann, J. Radiometric Comparison within the Sentinel-1 SAR Constellation over a Wide Backscatter Range. *Remote Sens.* **2020**, *12*, 854. https://doi.org/10.3390/rs12050854.
81. Schmidt, K.; Schwerdt, M.; Hajduch, G.; Vincent, P.; Recchia, A.; Pinheiro, M. Radiometric Re-Compensation of Sentinel-1 SAR Data Products for Artificial Biases due to Antenna Pattern Changes. *Remote Sens.* **2023**, *15*, 1377. https://doi.org/10.3390/rs15051377.
82. Sarabandi, K.; Chiu, T.C. Optimum Corner Reflectors for Calibration of Imaging Radars. *IEEE Trans. Antennas Propag.* **1996**, *44*, 1348–1361. https://doi.org/10.1109/8.537329.
83. Alpers, W.; Zhang, B.; Mouche, A.; Zeng, K.; Chan, P.W. Rain footprints on C-band synthetic aperture radar images of the ocean—Revisited. *Remote Sens. Environ.* **2016**, *187*, 169–185. https://doi.org/10.1016/j.rse.2016.10.015.
84. Crosetto, M.; Monserrat, O.; Cuevas-González, M.; Devanthéry, N.; Crippa, B. Persistent Scatterer Interferometry: A Review. *ISPRS J. Photogramm. Remote Sens.* **2016**, *115*, 78–89. https://doi.org/10.1016/j.isprsjprs.2015.10.011.
85. Liedel, N.; Ziemer, J.; Jänichen, J.; Schmullius, C.; Dubois, C. Novel Amplitude-Based Approach for Reducing Sidelobes in Persistent Scatterer Interferometry Processing Using Spatially Variant Apodization. *Sensors* **2026**, *26*, 204. https://doi.org/10.3390/s26010204.
86. Dai, K.; Deng, J.; Xu, Q.; Li, Z.; Shi, X.; Hancock, C.; Wen, N. Interpretation and Sensitivity Analysis of the InSAR Line-of-Sight to 3D Motion Components. *Int. J. Remote Sens.* **2022**, *43*, 5756–5785. https://doi.org/10.1080/15481603.2022.2100054.
87. SAR-MPC. Sentinel-1 Annual Performance Report 2024, Version 2.1; ESA SAR-Mission Performance Cluster: 31 January 2025. Available online: https://sentiwiki.copernicus.eu/__attachments/1681272/DI-MPC-APR-0715%20-%20Sentinel-1%20Annual%20Performance%20Report%202024%20-%202.1.pdf?inst-v=aa4d6a19-10ba-4d86-8ad9-b06c3f577f80 (accessed on 6 November 2025).
88. Meister, A.; Balasis-Levinsen, J.; Keller, K.; Pedersen, M.R.V.; Merryman Boncori, J.P.; Jensen, M. A Field Test of Compact Active Transponders for InSAR Geodesy. *J. Geodetic Sci.* **2024**, *14*, 20220164. https://doi.org/10.1515/jogs-2022-0164.

89. Luzi, G.; Espín-López, P.F.; Mira Pérez, F.; Monserrat, O.; Crosetto, M. A Low-Cost C-Band Active Reflector for InSAR Deformation Monitoring: Field Performance. *ISPRS Ann. Photogramm. Remote Sens. Spatial Inf. Sci.* **2024**, *XLVIII-3*, 319–326. https://doi.org/10.5194/isprs-archives-XLVIII-3-2024-319-2024.
90. Xia, Z.; Motagh, M.; Li, T. Performance Analysis of Dihedral Corner Reflectors for Slope Movements: A Case Study from Aniangzhai Landslide in China. *IEEE Geosci. Remote Sens. Lett.* **2022**, *19*, 4515605. https://doi.org/10.1109/LGRS.2022.3220649.
91. Rana, N.M.; Delaney, K.B.; Evans, S.G.; Deane, E.; Small, A.; Adria, D.A.M.; McDougall, S.; Ghahramani, N.; Take, W.A. Application of Sentinel-1 InSAR to Monitor Tailings Dams and Predict Geotechnical Instability: Practical Considerations Based on Case Study Insights. *Bull. Eng. Geol. Environ.* **2024**, *83*, 204. https://doi.org/10.1007/s10064-024-03680-3.
92. Alonso-Díaz, A.; Roque, D.; Lima, J.N.; Rodríguez, J.L.; Solla, M. Improvement of InSAR Displacements Based on GNSS Station Calibration over Corner Reflector. *Measurement* **2025**, *216*, 118946. https://doi.org/10.1016/j.measurement.2025.118946.
93. Fuhrmann, T.; Garthwaite, M.C.; McClusky, S. Investigating GNSS Multipath Effects Induced by Co-Located Radar Corner Reflectors. *J. Appl. Geod.* **2021**, *15*, 207–224. https://doi.org/10.1515/jag-2020-0040.
94. Crosetto, M.; Crippa, B.; Mróz, M.; Cuevas-González, M.; Shahbazi, S. Applications Based on EGMS Products: A Review. *Remote Sens. Appl. Soc. Environ.* **2025**, *37*, 101452. https://doi.org/10.1016/j.rsase.2025.101452.
95. Cigna, F.; Esquivel Ramírez, R.; Tapete, D. Accuracy of Sentinel-1 PSI and SBAS InSAR Displacement Velocities against GNSS and Geodetic Leveling Monitoring Data. *Remote Sens.* **2021**, *13*, 4800. https://doi.org/10.3390/rs13234800.
96. Sadeghi, Z.; Wright, T.J.; Hooper, A.J.; Jordan, C.; Novellino, A.; Bateson, L.; Biggs, J. Benchmarking and Inter-Comparison of Sentinel-1 InSAR Velocities and Time Series. *Remote Sens. Environ.* **2021**, *256*, 112306. https://doi.org/10.1016/j.rse.2021.112306.
97. Kalia, A.C. *Landslide Activity Detection Based on Nationwide Sentinel-1 PSI Datasets*; DGK, Series C, Heft 917; Bavarian Academy of Sciences and Humanities: Munich, Germany, 2023. Available online: https://publikationen.badw.de/de/049490097 (accessed on 5 November 2025).
98. Ferretti, A.; Savio, G.; Barzaghi, R.; Borghi, A.; Musazzi, S.; Novali, F.; Prati, C.; Rocca, F. Submillimeter Accuracy of InSAR Time Series: Experimental Validation. *IEEE Trans. Geosci. Remote Sens.* **2007**, *45*, 1142–1153. https://doi.org/10.1109/TGRS.2007.894440.
99. Collilieux, X.; Courde, C.; Fruneau, B.; Aimar, M.; Schmidt, G.; Delprat, I.; Defresne, M.-A.; Pesce, D.; Bergerault, F.; Wöppelmann, G. Validation of a Corner Reflector Installation at Côte d'Azur Multi-Technique Geodetic Observatory. *Adv. Space Res.* **2022**, *70*, 360–370. https://doi.org/10.1016/j.asr.2022.04.050.